https://doi.org/10.5194/essd-2026-334
Preprint. Discussion started: 22 June 2026

Agreement, opposition, and dataset influence in global evapotranspiration trends

Johanna Ruth Thomson[1], Yannis Markonis[1], Riya Dutta[2], Simone Fatichi[3], Martin Hanel[1], Akash Koppa[4], Petr Maca[1], Vishal Thakur[1], Mijael Rodrigo Vargas Godoy[5], and Athanasios Paschalis[6]

[1]Faculty of Environmental Sciences, Czech University of Life Sciences Prague, Kamýcká 129, Praha – Suchdol, Czech Republic

[2]Department of Environmental Science and Engineering, Indian Institute of Technology (ISM) Dhanbad, Dhanbad, India

[3]Department of Civil and Environmental Engineering, National University of Singapore, Singapore, Singapore

[4]Department of Environmental Science and Technology, University of Maryland, College Park, MD, USA

[5]Department of Physical Geography and Geoecology, Charles University, Prague, Czechia

[6]Department of Civil and Environmental Engineering, University of Cyprus, Nicosia, Cyprus

Correspondence: Johanna R. Thomson bloecher@fzp.czu.cz

Abstract. Evapotranspiration (ET) is a key component of the terrestrial water and energy balance, and numerous global gridded ET products are routinely used to assess historical variability and trends. However, differences in forcing data, model structure and physics in these products complicate robust ET trend analyses. Here, we present a systematic intercomparison of 14 global terrestrial ET datasets for the period 2000–2019. We introduce a topology framework that categorizes ET datasets according to their trend signatures within multi-product ensembles, providing insight into the structural role of each dataset and revealing how certain products consistently amplify or oppose dominant trends, patterns that are not evident from standard ensemble statistics. We find that products which amplify negative trends consistently oppose the dominant ensemble trend direction, whereas products that amplify positive trends tend to produce statistically significant trends where most datasets indicate weak or non-significant change. We quantify the magnitude, direction, and statistical significance of ET trends across products and evaluate their spatial consistency. The analysis reveals substantial divergence among datasets. While many products indicate predominantly positive ET trends, agreement on the magnitude and direction of change is lacking across many regions. In many regions, trends differ by more than an order of magnitude, and the spatial patterns of significant trends are highly product-dependent. The resulting harmonized trend estimates and classification provide a reference resource for evaluating current and future ET products, assessing uncertainty in trend studies, and guiding the use and improvement of ET datasets.

https://doi.org/10.5194/essd-2026-334
Preprint. Discussion started: 22 June 2026

More broadly, the topology framework can be extended beyond ET to geoscientific data product ensembles in general, enabling fitness for purpose evaluation, uncertainty assessment, and more systematic intercomparison across datasets.

1 Introduction

Evapotranspiration (ET) is a major component of the terrestrial water cycle and links the land surface to both the energy and carbon cycles (Wang and Dickinson, 2012; Good et al., 2015; Yang et al., 2023). Global gridded ET datasets derived from satellite observations, land surface models, and reanalysis products are widely used to investigate land–atmosphere interactions, evaluate land-surface-model behavior, and analyze variability and long-term trends in terrestrial water fluxes. As a result, these datasets form an important data foundation for studies of terrestrial hydrology and climate change, and differences among products can influence the interpretation or even direction of ET change. In the last two decades, progress in both physical and statistical modeling have led to the development of numerous multi-year global gridded ET data products which employ machine-learning (Elnashar et al., 2021; Li et al., 2024), reanalysis (Kobayashi et al., 2015; Muñoz-Sabater et al., 2021), remote-sensing (Martens et al., 2017; Zheng et al., 2022), hydrological and land surface models (LSM) (Beaudoing et al., 2020; McNally et al., 2017), and products upscaled from *in situ* FLUXNET (Pastorello et al., 2020) measurements (Jung et al., 2019). This growing diversity of products partly explains the dataset-dependent variability in ET trends discussed above. Despite their widespread use, the structural behavior of ET datasets in trend detection remains incompletely characterized. This study provides a systematic assessment of global gridded ET products with a focus on the consistency of recent ET trend estimates and the structural roles that individual datasets play within multi-product trend ensembles.

Global analyses of ET trends over the past two decades have produced divergent results. Several recent studies reported ET increases (Yang et al., 2023; Zhang et al., 2015, 2016, 2022; Tang et al., 2024) and in some cases even acceleration of ET(Yang et al., 2023), primarily attributed to greening due to the CO_2 fertilization effect, as well as intensified atmospheric moisture demand under warming. However, the reported global trends vary widely, partly because of differences in the time periods covered. For instance, large El Niño events can cause spikes in global ET. If the time period begins after a large El Niño event, such as the event in 1998, positive ET trend estimates can be lower or even negative as shown in Jung et al.(Jung et al., 2010). In addition to period sensitivity, trend estimates also depend strongly on dataset choice. While many studies report a global increase in ET, some recent findings reveal a more complex picture with certain ET data products producing negative global trends (Pan et al., 2020; Kim et al., 2021; Ruan et al., 2025). Recent work by Tang et al. (2024) further shows that ET products are often poorly temporally correlated. As a result, both the magnitude and direction of long-term ET trends remain uncertain, highlighting the need for systematic intercomparison and careful assessment of dataset-dependent variability. Existing comparisons typically quantify ensemble spread, but do not distinguish the structural roles that different data products play within the ensemble. As a result, a reproducible taxonomy of product behavior within ensembles is still missing.

While ET can be measured locally using various *in situ* methods, it cannot be directly observed at larger scales. Despite advances in remote sensing applications, accurate ET estimation remains challenging (McCabe et al., 2017; Miralles et al., 2016). Consequently, all ET products rely on empirical or process-based models to infer it indirectly (Wang and Dickinson, 2012).

https://doi.org/10.5194/essd-2026-334
Preprint. Discussion started: 22 June 2026

These data products employ different forcing data and land surface information, such as vegetation and soil properties, and use unique calibration approaches, contributing to substantial variations across products (Khan et al., 2018). In particular, the representation of plant transpiration, land cover effects, and soil hydraulic processes (Paschalis et al., 2022) remain a major source of uncertainty, with differences in vegetation parameterization causing vastly varying estimates of ET components (Miralles et al., 2016; Yang et al., 2023). All these factors contribute to an increasingly fragmented landscape of global ET data products, which undermines their robustness (Cai et al., 2024). This heterogeneity makes it likely that ET trend consistency varies across regions and not only globally, and that individual data products occupy distinct structural roles within trend ensembles. In this context, uncertainty in global ET trends remains substantial, making systematic multi-product intercomparison not only useful but necessary.

Validation of global gridded ET products remains challenging due to the limited availability and spatial coverage of direct observations. Most validation relies on comparison against *in situ* data, typically ET estimates derived from eddy covariance towers of the FLUXNET network (Pastorello et al., 2020), AmeriFlux including National Ecological Observatory Network (NEON), ChinaFLux, OZ-Flux, Integrated Carbon Observation System (ICOS). However, the use of *in situ* data for large-scale evaluation faces several well known limitations, including the well-known energy closure problem that makes quality of latent heat estimates from flux towers suboptimal for trend benchmarking (Mastrotheodoros et al., 2017; Mauder et al., 2020), limitations in extrapolating point-scale observations to larger areas due to land cover heterogeneity, topographic heterogeneity as flux towers are positioned in flat locations, scale-dependent processes at catchment or regional levels (Ershadi et al., 2014), and the frequent need for gap-filling. While gap-filling and data prolongation efforts exist (Li et al., 2025), around 90% of the eddy covariance sites are concentrated in Europe, North America, Australia and East Asia, predominantly China, (Pastorello et al., 2020), leaving large parts of the globe sparsely observed, including high ET regions such as the tropics. While water balance-based datasets, such as those developed by Ma et al. (2024), provide complementary validation for large river basins, helping to benchmark global ET products where flux-tower coverage is limited, they also suffer from assumptions on catchment storage dynamics. Therefore, the challenge of validating ET continues to hinder the ability to constrain ET estimates at global scale. As a result, uncertainty in long-term ET trend estimates remains substantial and proportionally much larger than uncertainty in precipitation (Beck et al., 2017; Gu and Adler, 2023; Gulev et al., 2023), underscoring the need for multi product intercomparison and more structured evaluation of product behavior within ensembles.

In this review, we assess the consistency and agreement of ET trends by harmonizing and analyzing fourteen publicly available global gridded ET products from 2000-2019. We quantify the extent to which products agree on trend magnitude, direction, and spatial patterns, both at the grid-scale and aggregated over reference regions defined by the Intergovernmental Panel on Climate Change (IPCC). To facilitate interpretation of inter-product differences, we introduce a classification framework of trend signature topologies, identifying which products amplify positive and negative trend signals, as well as those that systematically oppose the ensemble trend tendency. By combining comprehensive comparison with a conceptual classification framework, this study offers a resource for understanding uncertainty in ET trends and guides future analyses of global evapotranspiration.

https://doi.org/10.5194/essd-2026-334
Preprint. Discussion started: 22 June 2026

2 Methods

2.1 Evapotranspiration products

Products were selected to represent the major categories of currently available global ET datasets, including reanalysis, remote-sensing, land-surface-model, and composite products, while ensuring near-global terrestrial coverage and overlapping temporal availability for 2000–2019. These include,

- reanalysis products: ERA5-Land (Muñoz-Sabater et al., 2021), JRA-55 (Kobayashi et al., 2015), and MERRA-2 (Gelaro et al., 2017),
- remote-sensing-based products: BESS v2 (Li et al., 2023), ETmonitor (Zheng et al., 2022), GLEAM v4.1a (Miralles et al., 2025) , and MODIS 16A2 (Mu et al., 2011),
- land surface model-based products: FLDAS (McNally et al., 2017), GLDAS-CLSM v2.1 (Li et al., 2020), GLDAS-NOAH v2.1 (Beaudoing and Rodell, 2020), GLDAS-VIC v2.1 (Beaudoing et al., 2020) and TerraClimate (Abatzoglou et al., 2018) and
- composite products: CAMELE (Li et al., 2024) and SynthesizedET, (Elnashar et al., 2021),

thereby representing a wide range of existing ET estimates. Detailed metadata, including spatial and temporal resolution, are provided in Table 1, underlying schemes are provided in Table S1, data source of relevant variables are provided in Table S2. The data products are described in detail in Supporting Information (Supplementary Text S1).

All datasets were aggregated to annual totals and regridded to a common 0.25° × 0.25° grid using Climate Data Operators (CDO v2.0.4; (Schulzweida, 2023)). Unit conversions to millimeters were applied where necessary. Coarser-resolution products were downscaled using nearest-neighbor remapping, while finer-resolution products were upscaled via area-weighted averaging, both in geographic coordinates (EPSG:4326). Homogenization involved harmonizing units, aligning temporal coverage, and masking non-overlapping regions, following the procedure described in Vargas Godoy and Markonis (2023). The annual ET data was archived and is freely accessible at https://doi.org/10.5281/zenodo.18150992 (Thomson et al., 2026a) and can be also accessed by the open source evapoRe package (Ziveh et al., 2026). For grid-scale ensemble maps, only grid cells with data coverage from at least 13 of the 14 ET products were retained in order to maximize spatial coverage while preserving robust ensemble statistics. This mainly reduced inconsistencies in coastal boundaries and excluded Antarctica, large parts of Greenland, and open water bodies such as the Great Lakes. For direct product intercomparison and all aggregated regional analyses, including IPCC reference-region trends, only grid cells with complete coverage across all 14 products were used.

2.2 Trend estimates

Annual trends estimates, their p-values as well as their lower and upper bounds were obtained using block-bootstrapped Theil-Sen trends from the using `OpenAir` v2.18 (Carslaw and Ropkins, 2012) with blocks of 3 consecutive years and 599 repeats

Table 1. Overview of Datasets used in this study, including original spatial and temporal resolution and time period.

Dataset	*Spatial Resolution*	*Temporal Resolution*	*Time period*	*Reference*
ERA5-land	0.1°×0.1°	Monthly	1950 - present	Muñoz-Sabater et al. (2021)
JRA-55	0.57°×0.57°	Monthly	1958-2024	Kobayashi et al. (2015)
MERRA-2	0.5°×0.625°	Monthly	1980-present	Gelaro et al. (2017)
BESS v2	0.05°×0.05°	Daily	1982-2019	Li et al. (2023)
ETMonitor	1 km×1 km	Daily	2000-2019	Zheng et al. (2022)
GLEAM v4.1a	0.1°×0.1°	Daily	1980-2023	Miralles et al. (2025)
MODIS16A2	500 m×500 m	8-day	2000-present	Mu et al. (2011)
FLDAS	0.1°×0.1°	Monthly	1982-present	McNally et al. (2017)
GLDAS-CLSM v2.1	1.0°×1.0°	Monthly	2000-present	Li et al. (2020)
GLDAS-NOAH v2.1	0.25°×0.25°	Monthly	2000-present	Beaudoing and Rodell (2020)
GLDAS-VIC v2.1	1.0°×1.0°	Monthly	2000-present	Beaudoing et al. (2020)
TerraClimate	∼4 km×4 km	Monthly	1958-2019	Abatzoglou et al. (2018)
CAMELE	0.25°×0.25°	Monthly	2000-2020	Li et al. (2024)
SynthesizedET	1 km×1 km	Monthly	1982-2019	Elnashar et al. (2021)

to account for temporal autocorrelation. The block-bootstrap resampling was identical for all data products. All computations were performed in R (v4.2.2).

2.3 Stratification by climate and regions

Trend analyses were stratified across multiple environmental domains to capture spatial heterogeneity in evapotranspiration dynamics. We used (i) updated Intergovernmental Panel on Climate Change (IPCC) reference regions v4 (Iturbide et al., 2020) (Figure S1); (ii) evaporation quantiles based on the ET deciles of the ensemble mean (Figure S2) (iii) Köppen–Geiger climate classes (Beck et al., 2018) (Figure S3); and (iv) elevation classes adapted from Hersbach et al. (2020) (used as in Markonis et al. (2024)) (Figure S4).

2.4 Trend indices

2.4.1 Quartile ratio

In this study, the symmetric quartile ratio was calculated to reduce the influence of extreme trend estimates and provide a robust measure of variability across products. For each grid cell, the lower quartile (25th percentile, $Q25$) and upper quartile (75th percentile, $Q75$) of the trend estimates were computed with R base quantile function with type = 7, the default R method. These correspond approximately to the 4th–5th and 10th–11th ranks in the 14-member ensemble. The symmetric quartile ratio is defined as

$$R = \frac{\max(|Q75|,|Q25|)}{\min(|Q75|,|Q25|)}, \qquad (1)$$

which guarantees $R \geq 1$. This formulation removes sign information and reflects only the relative magnitude contrast between the quartiles. We used a ratio instead of calculating standardized interquartile range commonly used as a dataset disagreement metric (Markonis et al., 2024), because in our case the ensemble mean was often smaller than both $|Q25|$ and $|Q75|$ and in some grid cells was close to zero, artificially inflating this metric. The symmetric quartile ratio provides a more stable method for comparing grid cells with very different trend magnitudes and direction.

2.4.2 Uncertainty terminology

Trend estimates were classified as uncertain based on three criteria: magnitude, direction, or both.

- **Magnitude**: Local magnitude uncertainty was identified when the quartile ratio (Section 2.4.1) exceeded the global average of 3.3. This approach excludes extreme estimates and highlights regions with greater quartile ensemble spread than the global mean.
- **Direction**: Directional uncertainty was defined when $Q25$ and $Q75$ had opposite signs, indicating disagreement in trend direction. This criterion reduces the influence of small oscillating trends near zero.
- **Both**: Uncertainty in both was identified when both criteria were met.

2.4.3 Majority trend direction

The dataset concurrence index (DCI) (Anabalón and Sharma, 2017) represents the dominance of significant trend direction and is calculated as:

$$\mathrm{DCI} = \frac{N_{\mathrm{pos},s} - N_{\mathrm{neg},s}}{N}, \tag{2}$$

where $N_{\mathrm{pos},s}$ and $N_{\mathrm{neg},s}$ are the counts of positive and negative significant trends at a given grid cell, and N is the total number of evapotranspiration (ET) products. The subscript s indicates significant trends. The index ranges from -1 (all trends are significant and negative) to 1 (all trends are significant and positive). Intermediate values may result from a mix of positive and negative significant trends or from the presence of non-significant trends, making these values harder to interpret.

2.5 Topology framework

Here, we introduce a topology framework that allows defining data product roles within a multi-product context. The framework defines six categories based on trend signatures. These include three signal roles, namely “positive signal boosters”, “negative signal boosters” and “signal dampener”, and three opposition roles “trend opposer”, “opposition contributor” and “significance opposer”.

Trend signatures were derived by ranking the area fraction associated with each category for each product. Only grid cells with complete coverage across all data products were included. Each signature was evaluated across p-value thresholds of 0.01, 0.05, 0.1 and 0.2. For the main results, we use a p-value threshold of 0.05 for significant trends.

- Positive signal boosters: Data products were ranked according to the area fraction of their positive significant trends. A product with high rank amplifies the positive trend signal within the ensemble.
- Negative signal boosters: Data products were ranked according to the area fraction of their negative significant trends. A product with high rank amplifies the negative trend signal within the ensemble.
- Signal dampeners: Data products were ranked according to the area fraction of their non-significant trends. A product with high rank dampens the trend signal, typically because its variability is large relative to trend magnitude.
- Trend opposer: Data products were ranked according to the area fraction where the trend direction is different to the majority trend direction as defined by the DCI. A product with high rank most frequently opposes majority trend direction.
- Significance opposer: Data products were ranked according to the area fraction where a products opposes majority significance level. Opposition occurs when a product shows a significant trend while non-significant trends dominate, or vice versa. In this study, a product with high rank most often yields significant trends where non-significant trends dominate across the ensemble.
- Opposition contributor: Data products were ranked according to the area fraction where excluding that product removes opposition in trend direction in significant trends. A product with a high rank is therefore the sole source of directional opposition.

Examples of time series meeting these definitions are visualized in Fig. 1. These examples illustrate the conceptual behavior of each topology category within a multi-product ensemble.

3 Results

3.1 Global patterns of agreement and opposition in recent ET trends

The majority trend direction across the fourteen ET data products based on annual data from 2000-2019 is positive (Fig. 2 a) with substantial ensemble spread ranges from 4 mm yr^{-2} to -0.3 mm yr^{-2}. The upper quartile is approximately 3.3 larger than the lower quartile. Trend significance differs across products, 6 products estimate significant global positive trends at p-value of 0.05. The variation in block-bootstrapped upper and lower trend bounds (95 % confidence) highlights significant product-specific inter-annual variability. For instance, Synthesized ET (Elnashar et al., 2021) produced trend estimates with a lower bound of -2.4 and an upper bound 3.4 mm yr^{-2}. Apparently, even at the global scale, the consensus toward increasing ET is accompanied by substantial uncertainty in both trend magnitude and significance across products.

At the grid-scale, the majority trend direction, measured through dataset concurrence index, independent of significance, also remains positive with pockets of negative majority trend direction. An index value of 1 or -1 indicates complete agreement on positive or negative trends, respectively, while values near 0 reflect either equal positive and negative trends or absence of significance. When all trends are considered regardless of significance (Fig. 2, 72% of land show a positive trend majority

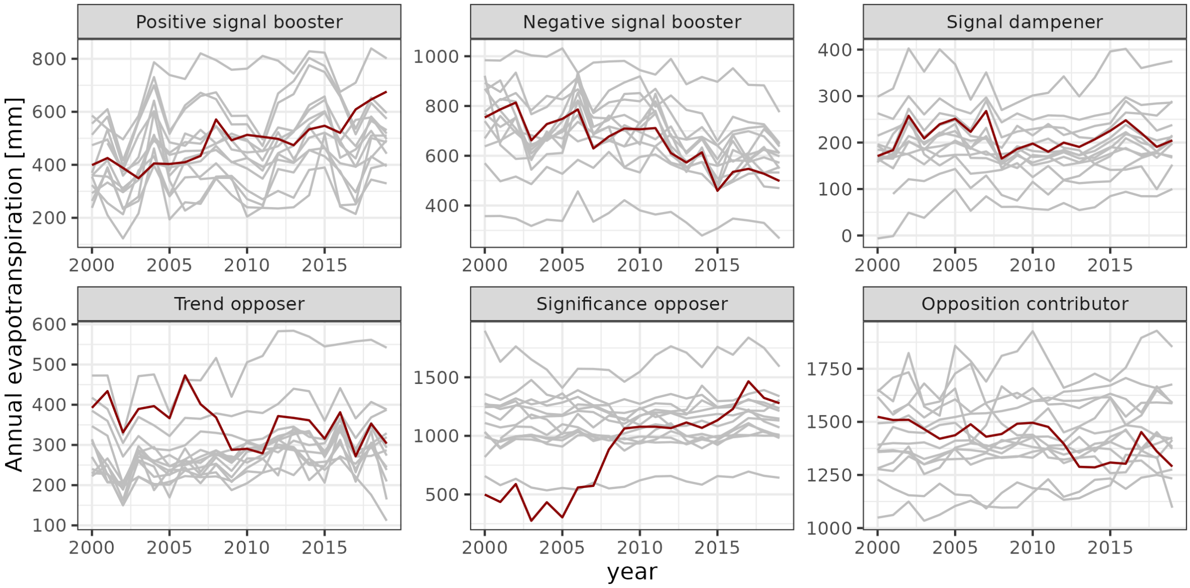

Figure 1. Examples of time series illustrating topology categories. The time series highlighted in red represents the dataset that fulfills the definition of the respective topology category, while the remaining ensemble members are shown in gray. The cases shown here represent illustrative examples and do not restrict the sign of the trend for opposition-based categories. In the examples shown, the positive signal booster exhibits a positive statistically significant trend, the negative signal booster exhibits a negative statistically significant trend, and the signal dampener exhibits a non-significant trend. The trend opposer exhibits a negative trend while the majority of ensemble members show a positive trend direction. The significance opposer exhibits a statistically significant trend while most ensemble members show non-significant trends. The opposition contributor exhibits a statistically significant negative trend while the remaining ensemble members show either positive significant or non-significant trends.

(red and orange), 22% a negative trend majority (blue), and 6.5% have no directional majority (gray). Lighter colors indicate a weaker majority. Strong majority (dark red and blue) was defined for values of 0.5, corresponding to more than 75 % of the products to share a common trend direction. Taken together, these results show that the predominance of positive ET trends is not only a global aggregate feature but also emerges across most land grid cells, although with substantial regional heterogeneity in the strength of agreement.

Trend magnitude varies substantially across products, and disagreement in direction is widespread (Fig. 2b. At the grid-scale trend estimates across products are less consistent than the global average, with the upper and lower quartile disagreeing on direction in almost half of the land indicating conflicting signals among ET products and reduced confidence in trend interpretation. Quartile uncertainty in trend magnitude is also quite pronounced: in 56% of the land, it is greater than the quartile ratio of global ET trends. This quartile uncertainty in magnitude is often very large, exceeding a 10-fold difference in about 20% of the land and a 20-fold difference in about 10% (Table S3). At the same time, approximately one third of terrestrial land exhibits quartile uncertainty in magnitude, while retaining a consistent trend direction, with over 84% of this area showing positive trends.

https://doi.org/10.5194/essd-2026-334
Preprint. Discussion started: 22 June 2026

Regions with low quartile uncertainty in both magnitude and direction ("None", ≈20%) allow identification of consistent ET trend patterns. Among these regions, nearly 78% share a positive trend, encompassing areas in North America (Alaska, western Canada, parts of the midwest, west, and southeast US), central-eastern and southern Europe (eastern Poland, parts of Croatia, Romania, Greece, Turkey), South Asia (western and northern India, Pakistan, eastern Iran), and eastern Asia (North China and Mongolia). The other 22% share negative trends include southern Africa (western South Africa, Namibia, parts of Mozambique), central Australia, the coastal area of northeastern Brazil, western Kazakhstan, and north of the Caspian Sea. These patterns show that robust spatial agreement in ET trends is limited to a relatively small fraction of land, whereas most regions are characterized by substantial uncertainty in either magnitude, direction, or both.

Disagreement in trend direction is very common and is not only limited to trends with weak signals. In fact, opposition in trend direction occur even among products with highly significant trends (p-values below 0.01). Figure 2c shows that such opposing trends at low p-values are particularly notable in equatorial regions, with clear clusters in the Congo and Amazon Basins. Other clusters appear in colder regions, such as around Hudson Bay, southern South America, Northern Europe, and temperate zones including Western Europe and regions east of the Black Sea. Many of these regions lack flux-tower stations and are therefore likely weakly constrained by direct measurements. They also overlap with areas showing weaker or absent majority trend direction. Opposition at low p-values is particularly meaningful because high variability in ET time series results in many non-significant trend estimates. Despite this, 76% of land exhibits at least one significant trend at $p \leq 0.05$ (Fig. S7). We can thus argue that directional disagreement is a structurally important feature of ET trend ensembles, occurring even where individual products indicate strong and highly significant trends.

These results indicate that positive ET trends are predominant, but their magnitudes vary substantially across data products. In nearly one fifth of all land areas, the lower and upper quartile trend estimates differ by more than a factor of ten, while nearly half of global land area shows directional disagreement between quartiles. The onset of opposition among significant trends also occurs for highly significant trends affecting mostly equatorial and cold regions. While these diagnostics reveal widespread disagreement at the grid scale, evapotranspiration trends are frequently interpreted at regional scales in climate assessments. Aggregating trends across spatially coherent regions therefore provides a complementary perspective on ensemble consistency and helps assess whether disagreement persists after spatial averaging.

Additional diagnostics supporting these findings, including spatial trend maps for all individual datasets (Figs. S5–S20) and agreement metrics (Figs. S21–S26), are provided in the Supplement.

3.2 Regional patterns of ET trends and ET trend uncertainty across IPCC reference regions

To assess ET trend consistency at regional scales, we analyze trends across the 44 reference regions defined by the Intergovernmental Panel on Climate Change (IPCC) Sixth Assessment Report (Fig. 3). These regions provide spatially coherent climate units commonly used in climate assessment studies and allow aggregation of grid-scale trends into regionally interpretable signals.

Even after aggregation to terrestrial IPCC reference regions, ET trend magnitude and direction remain strongly dataset-dependent (Fig. 3 a). While many regions exhibit relatively large trend magnitudes in at least some datasets, agreement in

https://doi.org/10.5194/essd-2026-334
Preprint. Discussion started: 22 June 2026

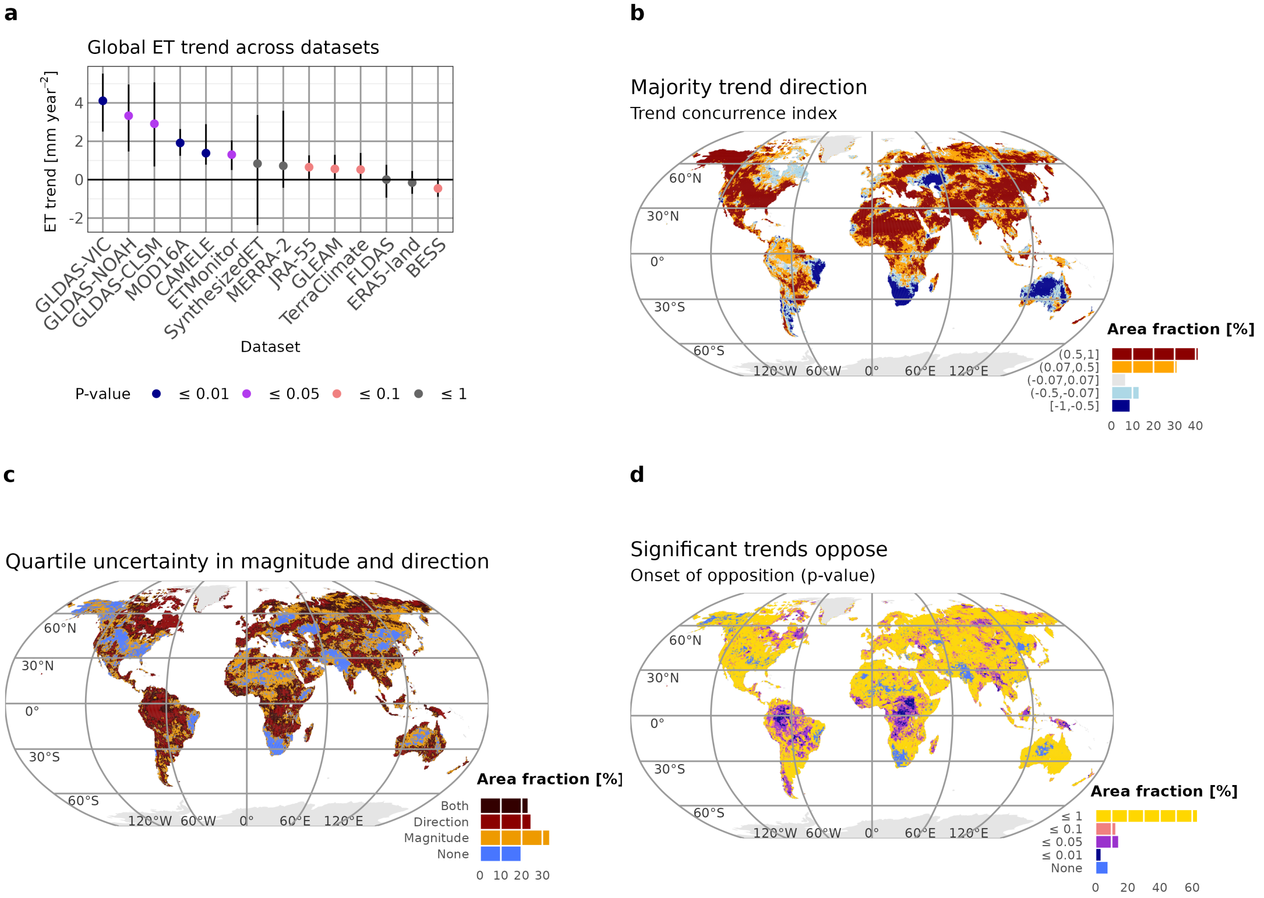

Figure 2. Variation in ET trends. (a) Variation of global annual trends across data sets including trend significance. The black line indicates the upper (95 %) and lower (5 %) trend bounds from block-bootstrap for BESS v2 (Li et al., 2023), CAMELE (Li et al., 2024), ERA5-land (Muñoz-Sabater et al., 2021), ETMonitor (Zheng et al., 2022), FLDAS (McNally et al., 2017), GLDAS-CLSM v2.1 (Li et al., 2020), GLDAS-NOAH v2.1 (Beaudoing and Rodell, 2020), GLDAS-VIC v2.1 (Beaudoing et al., 2020), GLEAM v4.1a (Miralles et al., 2025), JRA-55 (Kobayashi et al., 2015), MERRA-2 (Gelaro et al., 2017), MOD16A2 (Mu et al., 2011), SynthesizedET (Elnashar et al., 2021), TerraClimate (Abatzoglou et al., 2018). (b) Map of majority trend direction of all trends irrespective of their significance. Red indicates a positive direction and blue indicates a negative direction. Gray indicates an equal number of positive and negative trends.(c) Map of quartile uncertainty in magnitude and direction of global annual trends. (d) Map of p-value indicating onset of directional opposition of significant trends.

trend direction is limited. Products show complete agreement on trend direction in only four out of 44 IPCC reference regions, indicating that regional ET trend estimates remain sensitive to dataset selection. Statistical significance also varies markedly across regions. In most regions, individual datasets indicate differing directions of change, highlighting that regional ET trend estimates can vary depending on the dataset selected.

https://doi.org/10.5194/essd-2026-334
Preprint. Discussion started: 22 June 2026

The statistical significance of ET trends varies considerably across regions. Several regions exhibit relatively large trend magnitudes while simultaneously showing low statistical significance across many products, indicating that trend signals are often not strong across the products compared to the high variability in the annual time series.

Across Africa, ensemble trends range from -2.7 mm yr^{-2} in West Southern Africa (WSAF) to 3.4 mm yr^{-2} in Central Africa (CAF). The only region with complete directional agreement is Saharan Africa (SAH) with all data products indicating positive trends. Most trends remain non-significant across products in African regions despite relatively high magnitude estimates such as in WSAF with non-significant trends of up to -6.3 mm yr^{-2}. Exceptions include CAF with 9 products resulting in significant trend estimates (p-value < 0.05), generally agreeing on direction, except for FLDAS with significant negative trend of -5.1 mm yr^{-2}.

Across Asia, ensemble trends are positive in all regions and range from 0.7 mm yr^{-2} in the Arabian Peninsula (ARP) to 3.9 mm yr^{-2} in South East Asia (SEA). While the only region with complete directional agreement is East Central Asia (ECA) with consistent positive trends, positive trend direction dominates across all the continent, although significant directional opposition occurs in East Siberia (ESB). This comparatively strong agreement in parts of arid and semi-arid Asia is consistent with the broader climate-stratified analysis (Fig. S27), where arid Köppen–Geiger classes exhibit relatively low directional uncertainty. While ARP exhibits relatively consistent small trend magnitudes, large and significant trends are present in SEA with magnitudes reaching 21.2 mm yr^{-2} in GLDAS-CLSM v2.1. Sustained trends of this magnitude would correspond to cumulative ET changes exceeding 400 mm over two decades, implying potentially substantial impacts on regional water and energy balances. Such large long-term changes further emphasize the importance of carefully evaluating the plausibility and structural behavior of individual ET products, while illustrating how strongly individual datasets can diverge from the broader ensemble behavior.

Across Australasia, regions show weaker coherence. Ensemble trends range from -0.9 mm yr^{-2} in Central Australia (CAU) to 2.2 mm yr^{-2} in New Zealand (NZ) and no region exhibits complete directional agreement. Negative trends dominate Australasian IPCC reference regions except for NZ. Trends across Australasia are generally non-significant with the exception of two data products exhibiting significant positive trends in NZ, even resulting in a significant trend in the ensemble mean.

Across Europe, ensemble trends across regions are non-significant and range from -0.7 mm yr^{-2} in Eastern Europe (EEU) to 1.6 mm yr^{-2} in the Mediterranean (MED). Despite the relatively high number of *in situ* observations, there is no region with complete directional agreement and directional dominance is region dependent. Significant directional opposition is especially evident in Greenland-Iceland (GIC).

Across North and Central America, ensemble trends are positive and range from 0 mm yr^{-2} in North East North America (NEN) to 2.5 mm yr^{-2} in Caribbean (CAR). Regions with complete directional agreement include North Central America (NCA) and North-West North America (NWN) with consistent positive trends. While all trends are non-significant in NCA, nine products exhibit significant positive trends in NWN. Positive non-significant trends dominate North and Central American IPCC reference regions except for NEN where negative trends dominate and CAR where six products exhibit a negative trend exhibiting overall directional disagreement.

Finally, across South America, regions exhibit some of the strongest inter-product contrasts. Ensemble trends range from -3 mm yr^{-2} in North East South America (NES) to 2.4 mm yr^{-2} in North South America (NSA), but no region shows complete directional agreement, directional dominance is region dependent and significant directional opposition is common and present in NSA, North West South America (NWS), South American Monsoon (SAM), South South America (SSA). Across all IPCC reference regions, trend magnitudes vary the most in NSA ranging from 19.1 mm yr^{-2} to -12.7 mm yr^{-2}. These estimates imply extremely large cumulative long-term ET changes and illustrate the extent to which individual products can diverge in their representation of regional hydroclimatic change.

Overall, the regional analysis shows that spatial aggregation reduces some local scale noise, but substantial differences in ET trend magnitude, direction, and significance persist across products and continents.

Quartile uncertainty in both trend magnitude and direction is substantial in almost all IPCC reference regions (Fig. 3 b). Area fractions of low quartile uncertainty ("None") range from around 1% in NEN, NWS, GIC and NSA to over 40% in NWN, WSAF and CNA, with a mean area fraction of 17%. To fully describe the spatial extent of quartile, the category "Both", representing simultaneous uncertainty in magnitude and direction, should also be considered. Area fractions of magnitude uncertainty vary across IPCC reference regions, ranging from 26% in NEN to 84% in the Russian Far East (RFE). Half of all regions have magnitude uncertainty fractions between 49% and 63%. Quartile uncertainty in direction is similarly widespread, ranging from 22% in RFE and NWN to 91% in NEN. For 50% of all regions direction uncertainty covers between 37% and 61% of the area, indicating a slightly broader spread than in the magnitude uncertainty. Notably, some regions with small area fractions of magnitude uncertainty, such as GIC, NEN, NSA and NWS, can exhibit large fractions of direction uncertainty. Therefore, here, a small area fraction of magnitude uncertainty is not a sign of agreement in trends because it might coincide with substantial directional disagreement. Finally, the four regions with complete trend directional agreement SAH, ECA, NCA and NWN are also among the regions with the lowest area fraction in grid-scale quartile uncertainty in direction.

Quartile uncertainty in aggregated IPCC reference regions reveal a hemispheric contrast: low uncertainty regions are mainly located in the Northern Hemisphere and almost all regions with directional uncertainty in the Southern Hemisphere, together with cold polar regions and Eastern Europe (Fig. 3 c). There is no precise area fraction threshold that determines whether grid-wise quartile uncertainty translates into aggregated quartile uncertainty. We can observe a tendency for regions with higher area fractions of low uncertainty (“None”) to also show low aggregated quartile uncertainty. Examples include Africa: WSAF, SAH; Asia: SAS, WCA; Europe: WCE; North and Central America: NWN, CNA, ENA, ENA, NCA; South America: NES).

Grid-scale quartile uncertainty can affect large area fractions even when the aggregated regional estimate shows quartile agreement both in trend direction and magnitude. This reflects the effect of spatial smoothing across large and climatically meaningful regions, which can decrease ensemble spread and increase the apparent robustness of the regional mean. We can identify regions such as CAF in Africa where the area fraction of direction and magnitude uncertainty reaches 95%, but this strong local disagreement is not evident in the aggregated estimate.

To complement quartile uncertainty across IPCC reference regions, area fractions of grid-scale quartile uncertainty across environmental gradients, namely ET quantiles, elevation classes, latitudinal classes and main Koeppen-Geiger climate classes were also estimated (Figure S27). Along these gradients, direction uncertainty shows the clearest structure: it increases across

https://doi.org/10.5194/essd-2026-334
Preprint. Discussion started: 22 June 2026

ET quantiles and decreases with elevation, except above 3000 m. It is also highest in equatorial latitudes and Koeppen-Geiger climate class and northern latitudes and polar climates. By contrast, magnitude uncertainty remains relatively stable across these gradients. Higher magnitude uncertainty can be observed for lowest ET quantiles and southern most latitudinal band. The area affected by simultaneous uncertainty in magnitude and direction largely follows the same pattern as direction uncertainty. Consequently, areas of low uncertainty follow the inverse shape of direction uncertainty with negligible area fractions of low uncertainty in highest ET quantile, 3000m + and polar and equatorial climates.

Regional patterns also differ markedly across continents. Africa and South America show some of the largest disagreement, combining wide spreads in trend magnitude and direction. Asia is more consistently characterized by positive ensemble trends, although full directional agreement remains rare. Australasia is dominated by negative trends except for New Zealand, but most trends are not statistically significant. Europe displays generally weak and mixed trends, with no region exhibiting complete directional agreement. North and Central America show the clearest regional coherence towards positive trends, including two regions with complete agreement in trend direction. Overall, spatial aggregation to IPCC regions reduces local scale complexity but does not remove substantial inter-product differences in regional ET trend estimates.

Overall, the regional analysis shows that aggregation to IPCC reference regions reduces some grid-scale variability but does not eliminate disagreement among evapotranspiration products. Complete directional agreement across all datasets occurs in only four regions, while most regions exhibit differing trend directions among products. Large trend magnitudes are common across regions, yet statistically significant trends remain relatively rare and unevenly distributed across the ensemble. Notably, directional disagreement persists even among statistically significant trends in several regions including Central Africa, Eastern Siberia, Greenland–Iceland, and multiple South American regions. Quartile diagnostics reinforce this interpretation by further indicating that direction uncertainty varies more strongly across regions than magnitude uncertainty, with substantial fractions of land area exhibiting opposing trend signs between quartiles. These results highlight that regional ET trend estimates remain sensitive to dataset choice even after spatial aggregation. To better understand how individual datasets contribute to regional agreement and disagreement within the ensemble, we next apply the trend topology framework to characterize the structural roles of products in shaping ensemble trend signals.

3.3 Global topology of ET product roles

To capture the contribution of individual ET data products to the overall trend signal and uncertainty, we explore how their trends behave compared to the rest of the dataset ensemble (Fig. 4). The six categories consist of three metrics to represent trend signal “positive signal boosters”, “negative signal boosters”, and “signal dampeners” and three metrics representing opposition, namely “opposition contributor”, “trend opposer”, “significance opposer”.

The topology analysis reveals several recurring product roles. Products that appear as strong trend opposers and opposition contributors also tend to emerge as negative signal boosters. In practice, these datasets contribute a large fraction of significant negative trends and frequently generate negative trends in grid cells where the ensemble majority indicates positive trends. In addition, these products often initiate directional opposition within the ensemble. Notable examples in this category include BESS v2, SynthesizedET, FLDAS, JRA-55, ERA5-Land and MERRA-2. Several of these datasets, particularly BESS v2,

https://doi.org/10.5194/essd-2026-334
Preprint. Discussion started: 22 June 2026

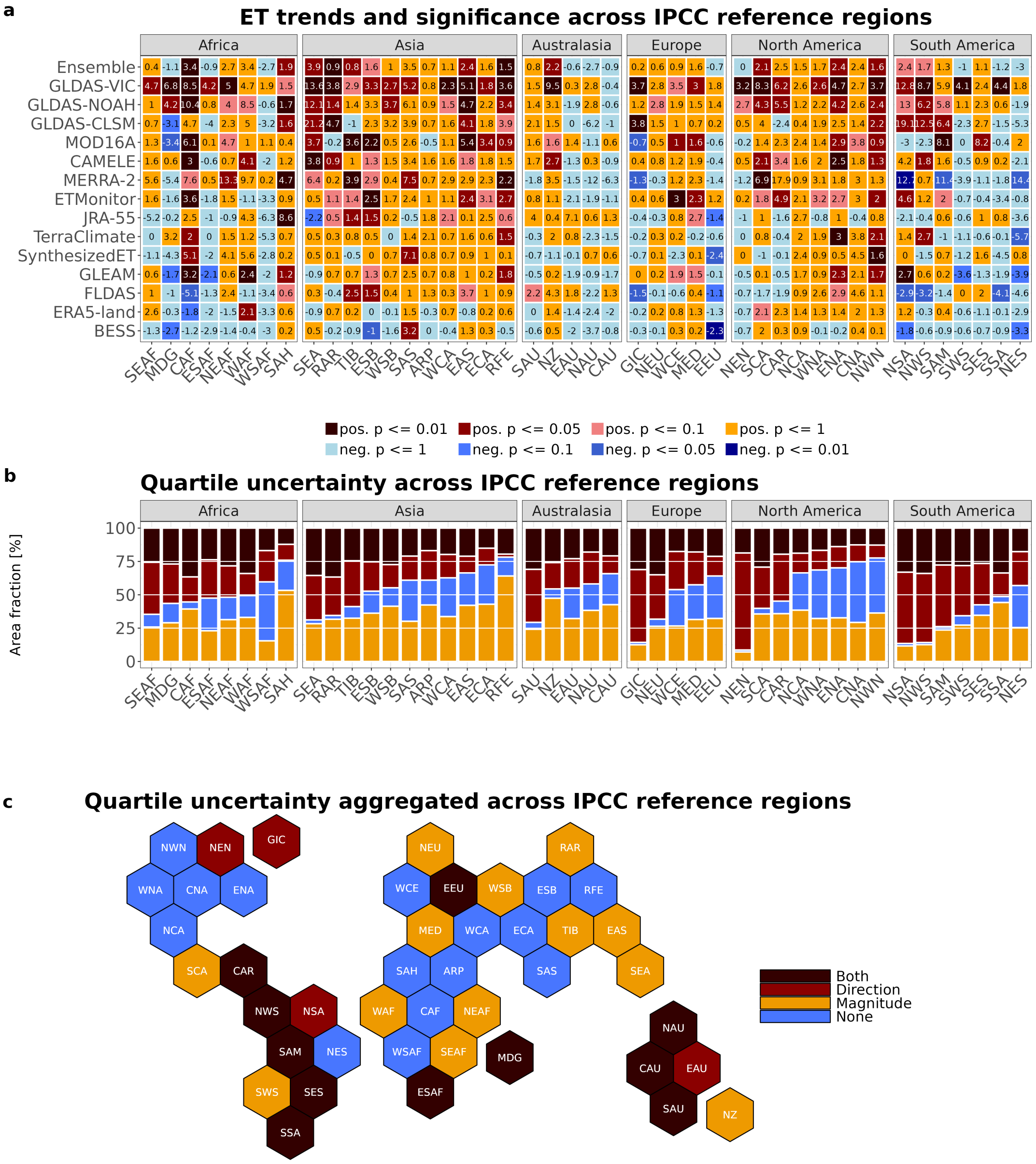

ET trends and significance across IPCC reference regions

Africa

	SEAF	MDG	CAF	ESAF	NEAF	WAF	WSAF	SAH
Ensemble	0.4	-1.1	3.4	-0.9	2.7	3.4	-2.7	1.9
GLDAS-VIC	4.7	6.8	8.5	4.2	5	4.7	1.9	1.5
GLDAS-NOAH	1	4.2	10.4	0.8	4	8.5	-0.6	1.7
GLDAS-CLSM	0.7	-3.1	4.7	-4	2.3	5	-3.2	1.6
MOD16A	1.3	-3.4	6.1	0.1	4.7	1	1.1	0.4
CAMELE	1.6	0.6	3	-0.6	0.7	4.1	-2	1.2
MERRA-2	5.6	-5.4	7.6	0.5	13.3	9.7	0.2	4.7
ETMonitor	1.6	-1.6	3.6	-1.8	1.5	-1.1	-3.3	0.9
JRA-55	-5.2	-0.2	2.5	-1	-0.9	4.3	-6.3	8.6
TerraClimate	0	3.2	2	0	1.5	1.2	-5.3	0.7
SynthesizedET	-1.1	-4.3	5.1	-2	4.1	5.6	-2.8	0.2
GLEAM	0.6	-1.7	3.2	-2.1	0.6	2.4	-2	1.2
FLDAS	1	-1	-5.1	-1.3	2.4	-1.1	-3.4	0.6
ERA5-land	2.6	-0.3	-1.8	-2	-1.5	2.1	-3.3	0.6
BESS	-1.3	-2.7	-1.2	-2.9	-1.4	-0.4	-3	0.2

Asia

	SEA	RAR	TIB	ESB	WSB	SAS	ARP	WCA	EAS	ECA	RFE
Ensemble	3.9	0.9	0.8	1.6	1	3.5	0.7	1.1	2.4	1.6	1.5
GLDAS-VIC	13.6	3.8	2.9	3.3	2.7	5.2	0.8	2.3	5.1	1.8	3.6
GLDAS-NOAH	12.1	1.4	1.4	3.3	3.7	6.1	0.9	1.5	4.7	2.2	3.4
GLDAS-CLSM	21.2	4.7	-1	2.3	3.2	3.9	0.7	1.6	4.1	1.8	3.9
MOD16A	3.7	-0.2	3.6	2.2	0.5	2.6	-0.5	1.1	5.4	3.4	0.9
CAMELE	3.8	0.9	1	1.3	1.5	3.4	1.6	1.6	1.8	1.8	1.5
MERRA-2	6.4	0.2	3.9	2.9	0.4	7.5	0.7	2.9	2.9	2.3	2.2
ETMonitor	0.5	1.1	1.4	2.5	1.7	2.4	1	1.1	2.4	3.1	2.7
JRA-55	-2.2	0.5	1.4	1.5	0.2	-0.5	1.8	2.1	0.1	2.5	0.6
TerraClimate	0.5	0.3	0.8	0.5	0	1.4	2.1	0.7	1.6	0.6	1.5
SynthesizedET	0.5	0.1	-0.5	0	0.7	7.1	0.8	0.7	0.9	1	0.1
GLEAM	-0.9	0.7	0.7	1.3	0.7	2.5	0.7	0.8	1	0.2	1.8
FLDAS	0.3	-0.4	2.5	1.5	0.4	1	1.3	0.3	3.7	1	0.9
ERA5-land	-0.9	0.7	0.2	0	-0.1	1.5	-0.3	0.7	-0.8	0.2	0.6
BESS	0.5	-0.2	-0.9	-1	-1.6	3.2	0	-0.4	1.3	0.3	-0.5

Australasia

	SAU	NZ	EAU	NAU	CAU
Ensemble	0.8	2.2	-0.6	-2.7	-0.9
GLDAS-VIC	1.5	9.5	0.3	2.8	-0.4
GLDAS-NOAH	1.4	3.1	-1.9	2.8	-0.6
GLDAS-CLSM	2.1	1.5	0	-6.2	-1
MOD16A	1.6	1.6	1.4	-1.1	0.6
CAMELE	1.7	2.7	-1.3	0.3	-0.9
MERRA-2	-1.8	3.5	-1.5	-12	-6.3
ETMonitor	0.8	1.1	-2.1	-1.9	-1.1
JRA-55	4	0.4	7.1	0.6	1.3
TerraClimate	-0.3	2	0.8	-2.3	-1.5
SynthesizedET	-0.7	-1.1	-0.1	0.7	0.6
GLEAM	-0.5	0.2	-1.9	-0.9	-1.7
FLDAS	2.2	4.3	1.8	-2.2	1.3
ERA5-land	0	1.4	-1.4	-2.4	-2
BESS	-0.6	0.5	-2	-3.7	-0.8

Europe

	GIC	NEU	WCE	MED	EEU
Ensemble	0.2	0.6	0.9	1.6	-0.7
GLDAS-VIC	3.7	2.8	3.5	3	1.8
GLDAS-NOAH	1.2	2.8	1.9	1.5	1.4
GLDAS-CLSM	3.8	1.5	1	0.7	0.2
MOD16A	-0.7	0.5	1	1.6	-0.6
CAMELE	0.4	0.8	1.2	1.9	-0.4
MERRA-2	-1.3	-0.3	1.2	2.3	-1.4
ETMonitor	0.4	0.6	3	2.3	1.2
JRA-55	-0.4	-0.3	0.8	2.7	-1.4
TerraClimate	-0.2	0.3	0.2	-0.2	-0.6
SynthesizedET	-0.7	0.1	-2.3	0.1	-2.4
GLEAM	0	0.2	1.9	1.5	-0.1
FLDAS	-1.5	-0.1	-0.6	0.4	-1.1
ERA5-land	-0.2	0.2	0.8	1.3	-1.3
BESS	-0.3	-0.1	0.3	0.2	-2.3

North America

	NEN	SCA	CAR	NCA	WNA	ENA	CNA	NWN
Ensemble	0	2.1	2.5	1.5	1.7	2.4	2.4	1.6
GLDAS-VIC	3.2	8.3	6.2	2.6	2.6	4.7	2.7	3.7
GLDAS-NOAH	2.7	4.3	5.5	1.2	2.2	4.2	2.6	2.4
GLDAS-CLSM	0.5	4	-2.4	0.4	1.9	2.5	1.4	2.2
MOD16A	-0.2	1.4	2.3	2.4	1.4	2.9	3.8	0.9
CAMELE	0.5	2.1	3.4	1.6	2	2.5	1.8	1.3
MERRA-2	-1.2	6.9	17.9	0.9	3.1	1.8	3	1.3
ETMonitor	0.2	1.8	4.9	2.1	3.2	2.7	3	2
JRA-55	-1	1	-1.6	2.7	-0.8	1	-0.4	0.8
TerraClimate	0	0.8	-0.4	2	1.9	3	3.8	2.1
SynthesizedET	0	-1	-0.1	2.4	0.9	0.5	4.5	1.6
GLEAM	-0.5	0.1	-0.5	1.7	0.9	2.3	2.1	1.7
FLDAS	-0.7	-1.7	-1.9	0.9	2.6	2.9	4.6	1.1
ERA5-land	-0.7	2.1	2.3	1.4	1.3	1.4	2	1.3
BESS	-0.7	2	0.3	0.9	-0.1	-0.2	0.4	0.1

South America

	NSA	NWS	SAM	SWS	SES	SSA	NES
Ensemble	2.4	1.7	1.3	-1	1.1	-1.2	-3
GLDAS-VIC	12.8	8.7	5.9	4.1	2.4	4.4	1.8
GLDAS-NOAH	13	6.2	5.8	1.1	2.3	0.6	-1.9
GLDAS-CLSM	19.1	12.5	6.4	-2.3	2.7	-1.5	-5.3
MOD16A	-3	-2.3	8.1	0	8.2	-0.4	2
CAMELE	4.2	1.8	1.6	-0.5	0.9	0.2	-2.1
MERRA-2	12.7	0.7	11.4	-3.9	-1.1	-1.8	14.4
ETMonitor	4.6	1.2	2	-0.7	-0.4	-3.4	-0.8
JRA-55	-2.1	-0.4	0.6	-0.6	1	0.8	-3.6
TerraClimate	1.4	2.7	-1	-1.1	-0.6	-0.1	-5.7
SynthesizedET	0	-1.5	0.7	-1.2	1.6	-4.5	0.8
GLEAM	2.7	0.6	0.2	-3.6	-1.3	-1.9	-3.9
FLDAS	-2.9	-3.2	-1.4	0	2	-4.1	-4.6
ERA5-land	1.2	-0.3	0.4	-0.6	-1.1	-0.1	-2.9
BESS	-1.8	-0.6	-0.9	-0.6	-0.7	-0.9	-3.3

Quartile uncertainty across IPCC reference regions

Quartile uncertainty aggregated across IPCC reference regions

Figure 3. ET trends and quartile uncertainty across IPCC reference regions. (a) Annual ET trend estimates in mm yr^{-2} were calculated from annual data covering 2000-2019 for the ensemble and for BESS v2, CAMELE, ERA5-land, ETMonitor, FLDAS, GLDAS-CLSM v2.1, GLDAS-NOAH v2.1, GLDAS-VIC v2.1, GLEAM v4.1a, JRA-55, MERRA-2, MOD16A2, SynthesizedET, and TerraClimate. Ensemble trends were estimated based on the time series of the ensemble mean where all products were weighted equally. The data products are ordered by mean trend magnitude, with the dataset with the highest positive trend shown at the top. (b) Area fraction of grid-scale quartile uncertainty in trend direction, magnitude, both or none. The IPCC reference regions in a and b are ordered by their area fraction of quartile uncertainty, with the IPCC reference region with highest area fraction listed first. (c) Hexagon map of IPCC reference region with quartile uncertainty using aggregated trend estimates from a. Central American IPCC reference regions were grouped with North America.

SynthesizedET, FLDAS, JRA-55, ERA5-Land also rank among the strongest signal dampeners, showing the highest area fraction of grids with non-significant trend. Together, these patterns indicate that products driving ensemble opposition are often also those that weaken the overall strength and coherence of the trend signal.

In contrast, most of the strongest positive signal boosters show a different pattern. These products tend to act as strong significance opposers, while remaining weak as trend opposers and opposition contributors. Rather than opposing the dominant trend direction, they frequently yield statistically significant trends in locations where the majority of datasets indicate non-significant trends. Examples include GLDAS-VIC v2.1, GLDAS-NOAH v2.1, MOD16A2, and ETMonitor. Interestingly, none of the top positive signal boosters are reanalysis products (Fig 4). This contrast highlights an important asymmetry in ensemble behavior: products that amplify negative signals often do so by opposing the dominant trend direction, whereas products that amplify positive signals mainly strengthen significance rather than alter direction.

Some datasets exhibit mixed roles that deviate from these broader patterns. MERRA-2, for example, appears both as a significance opposer, but acts as a negative signal booster indicating that it contributes negative trends while also producing statistically significant trends in locations where the ensemble signal is weak. GLDAS-VIC v2.1 shows a different type of mixed behavior: although it ranks among the strongest positive signal boosters, it also appears as a strong opposition contributor, producing significant positive trends in locations where other products indicate significant negative trends. GLEAM and TerraClimate are both signal dampers. In the case of TerraClimate, this role is especially clear, as it also appears among the weakest signal boosters while showing little tendency either to oppose majority significance or to contribute to broader opposition. GLEAM manifests a more medium rank in signal strength, also reflected in slightly stronger signals in oppositional categories. These mixed cases illustrate that product roles cannot always be reduced to a simple contrast between boosters and opposers, but instead span a wider range of structural behaviors within the ensemble.

Global trend signatures across data products reveal that while most outliers and trend direction opposers are negative signal boosters, positive signal boosters generate significant trends where the majority does not. ET products differ substantially in both the spatial distribution and area fraction of significant trends. To evaluate the robustness of these roles, the topology metrics were evaluated across multiple significance thresholds (Fig. S28). The overall product roles remain largely consistent across p-value thresholds, indicating that the identified patterns are relatively stable. Still, some changes in metric strength are observed. For example, the opposition contributor metric becomes stronger with increasing p-value thresholds for BESS v2 and SynthesizedET, while it weakens for GLDAS-NOAH v2.1. Similarly, the strength of the significance opposer metric decreases with increasing thresholds for some datasets (e.g., GLDAS-CLSM v2.1) and increases for others (e.g., JRA-55). These sensitivity tests imply that while the intensity of individual roles may shift with the significance threshold, the broader topology of product behavior remains robust.

3.4 Variability of ET product roles across reference regions

To evaluate whether the dataset roles identified in the global topology are preserved at regional scales, we examine topology patterns across three representative IPCC reference regions: the South American Monsoon (SAM), the Tibetan Plateau (TIB), and Western Central Europe (WCE) (Fig. 5). These regions were selected to capture different levels of ensemble disagreement,

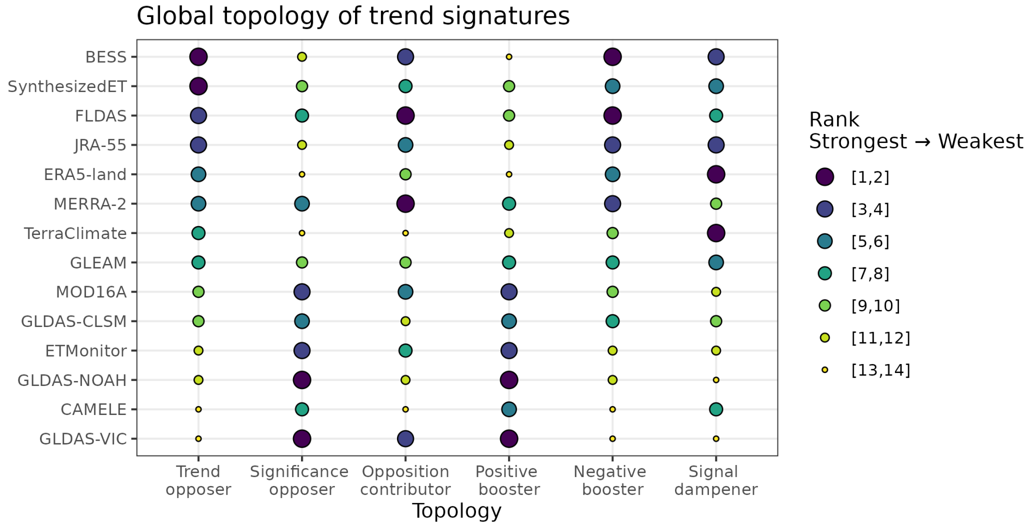

Figure 4. Global topology of trend signatures. Darker color and larger circles indicate a stronger signature of a given role. Datasets are ordered according to their rank as "Trend opposers", highlighting products that most frequently deviate from the majority trend direction across the ensemble

trend direction and environmental conditions. To facilitate comparison between global and regional dataset roles, datasets are ordered according to their global rank as trend opposers (Fig. 4).

Figure 5 shows that dataset roles vary across regions, indicating that ensemble behavior is partly region dependent. In particular, the strength of the trend opposer role differs between regions. For example, ERA5-Land does not act as a trend opposer in WCE, and MERRA-2 shows little trend opposer behavior in TIB. The selected regions were chosen to represent contrasting environmental conditions and levels of ensemble disagreement, and illustrate how the strength of topology roles can shift geographically. Some datasets, such as ERA5-Land, MERRA-2 and TerraClimate, exhibit substantial regional variation in their tendency to amplify or oppose dominant trend signals. By contrast, BESS v2, SynthesizedET, and FLDAS more consistently appear as negative signal boosters and trend opposers across the selected regions, although the strength of these roles still varies geographically.

Datasets acting as positive signal boosters tend to show stable significance opposer behavior across regions. Products such as MOD16A2, ETMonitor, GLDAS-NOAH v2.1, CAMELE, and GLDAS-VIC v2.1 consistently generate significant trends in locations where the ensemble majority indicates weaker or non-significant trends. Only a small number of datasets departs from this pattern. For example, GLDAS-CLSM shifts roles in TIB, where it becomes a stronger negative signal booster and contributes more strongly to directional opposition. Similarly, MERRA-2 shows weaker significance opposer behavior in WCE, coinciding with an increased signal dampener role.

Regional variation is also evident in the opposition contributor behavior, although it generally retraces the pattern of negative signal booster role. As observed in the global topology, exceptions occur for datasets such as GLDAS-VIC v2.1, which contributes to opposition onset despite functioning primarily as a positive signal booster. MERRA-2 also deviates from the general pattern in TIB, where it shows a stronger positive signal booster role. Such exceptions become especially pronounced in regions with dominant negative trends such as in NES. There, GLDAS-VIC, ETMonitor and MOD16A act as strong opposition contributors and even trend opposers, while also exhibiting a stronger positive signal booster role.

A different type of behavior is seen in data products that maintain intermediate positions across regions. GLEAM, for example, does not appear among the strongest signal boosters or opposers, but instead occupies mid-range ranks across the topology metrics both globally and regionally. Its opposition-related metrics, including trend opposer and opposition contributor, also remain within moderate ranks rather than showing weak values. This indicates that GLEAM participates in ensemble disagreement without systematically amplifying or dampening the dominant trend signal. As a result, its behavior remains relatively stable across the analyzed IPCC reference regions.

Overall, the regional topology analysis indicates that while the strength of individual dataset roles can vary across regions, several structural relationships remain consistent. Negative signal boosters tend to act as trend opposers and opposition contributors, whereas positive signal boosters frequently appear as significance opposers. At the same time, the regional variations highlight that dataset contributions to ensemble trend signals are not fixed, but can depend on geographic context. A complete overview of topologies across IPCC reference regions grouped by continent can be found in the Supplement (Figs. S29-S34).

3.5 Topology use case: Mapping where GLEAM most strongly opposes the majority trend

As a practical illustration of the topology framework, we examine where GLEAM v4.1a most strongly opposes the majority ensemble trend direction. In the global topology, GLEAM occupies mostly intermediate ranks across the topology metrics rather than emerging as a strong signal booster or opposer. This behavior is broadly consistent with its widespread use as a benchmark-type product in hydroclimatic studies. At the same time, its relatively balanced global position makes it a useful case study for illustrating how datasets that appear globally moderate can still exhibit strong regional disagreement with the ensemble.

This regional structure is clearly visible in Figure 6, which shows that GLEAM opposition to the ensemble majority is not spatially uniform, but concentrated in a limited number of regions. The strongest opposition of GLEAM to the ensemble majority occurs in Northern Europe (NEU) and South West South America (SWS), with additional high-ranking opposition in West North America (WNA), North Central America (NCA), South Central America (SCA), North East Africa (NEAF), East South Africa (ESAF), and East Central Asia (ECA). In these regions, GLEAM more frequently assigns a trend direction opposite to that supported by most of the other ET products. For example, in a region where the ensemble is dominated by positive ET trends, GLEAM may instead indicate decreasing ET, or vice versa. Thus, although GLEAM is not globally identified as a strong trend opposer, it becomes regionally important where its trend direction persistently diverges from the ensemble consensus.

This has direct implications for interpretation. If a study were to rely only on GLEAM in NEU or SWS, it could infer a regional ET tendency that differs from the one suggested by most other datasets. In practice, this means that conclusions about evaporation intensification, drying-related decline, or broader changes in land-atmosphere interactions could become highly dataset-dependent, and would require support from additional and alternative local data or mechanistic explanations to be

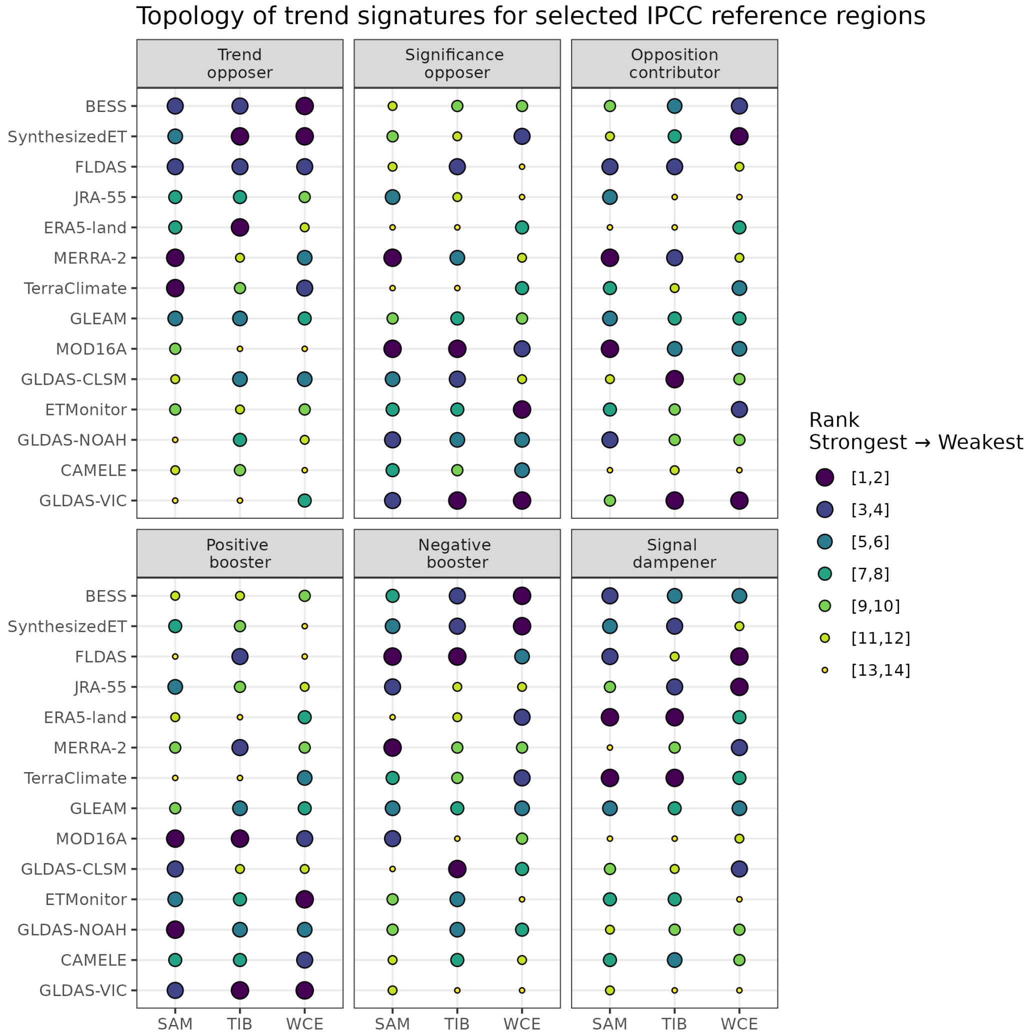

Figure 5. Topology of trend signatures for three IPCC reference regions South American Monsoon (SAM), Tibetan Plateau (TIB) and West-Central Europe (WCE). Dark color and larger radius indicate a stronger trend signature for a given category. Datasets are ordered according to trend opposer of the global topology.

trusted. The issue is especially important in regions where quartile diagnostics already indicate substantial directional uncertainty, because in such cases GLEAM is not simply one dataset among many, but one that may actively push the interpretation away from the ensemble majority. Conversely, in regions where GLEAM shows weak opposition, its use as a representative single-product choice may be more defensible. 430

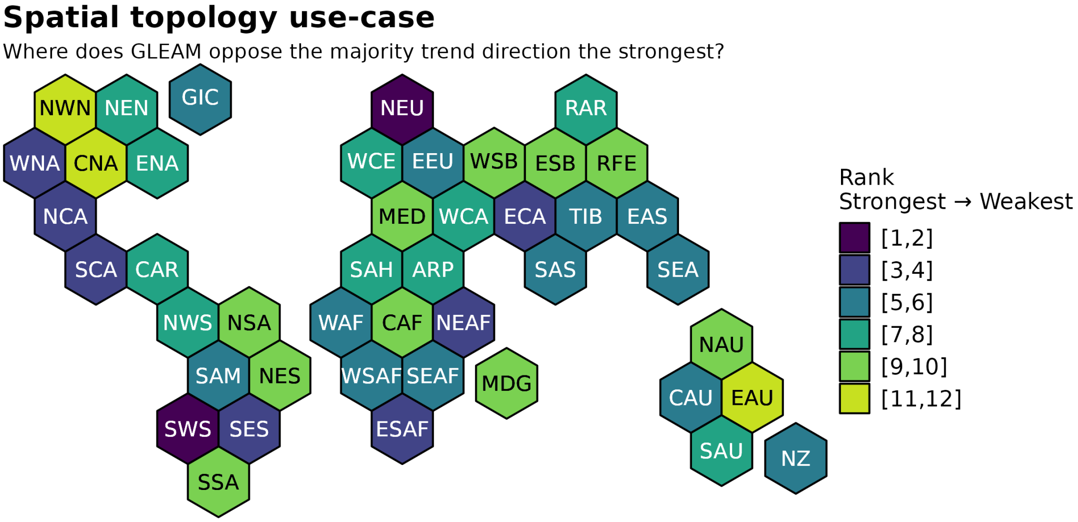

Figure 6. Where does GLEAM 4.1a oppose majority trend direction the most?

4 Discussion and conclusions

This study provides a harmonized assessment of ET trend estimates across 14 widely used global data products for 2000–2019. To achieve this we introduce a topology guided framework to diagnose how individual datasets behave within a multi product ensemble. The results show that recent ET trend estimates are strongly dataset-dependent even after harmonization to a common spatial and temporal framework.

At the global scale, the majority trend direction is positive, with 72% of land showing a positive trend majority, 22% showing a negative majority, and 6.5% showing no majority at all. However, this apparent large-scale coherence conceals substantial disagreement across products in both trend magnitude and direction. At the grid scale, the upper and lower quartile trends disagree in sign over 47% of land, while magnitude uncertainty exceeds the global quartile ratio over 56% of land. In nearly one fifth of land areas, the lower and upper quartile trends differ by more than a factor of ten. Thus, despite a dominant positive global tendency, the evident disagreement in quartile sign and magnitude underscores that ensemble behavior can be strongly influenced by the dataset selection. Most importantly, the topology analysis shows that disagreement is structured rather than random. Some products repeatedly act as negative signal boosters and trend opposers, whereas others behave as positive signal boosters that generate significance where the ensemble majority remains weak. This reveals that these products differ not only in their estimated ET, but also in their structural roles within the ensemble. Knowledge of these ensemble roles can help interpret ET trend analyses based on individual products.

Some broad features of the results are consistent with prior expectations. The domination of positive ET trends globally and across many regions, particularly in parts of Asia, North America, and several mid-latitude regions, has been reported in many studies (Yang et al., 2023; Zhang et al., 2015, 2016, 2022). Still, some of our findings are unexpected. For instance, disagreement is not confined to weak or marginal signals, but opposing trends occur even at very low p-values, especially in equatorial and cold regions. A direct implication of this is that statistical significance cannot necessarily be interpreted to inter-product consistency. What is also quite striking is that substantial disagreement is observed in data-rich regions; significant diverging trends appear across North America and Europe. Moreover, regional aggregation reduces some local variability, but does not resolve the disagreement as complete directional agreement is found in only 4 IPCC reference regions. This structured product dependence also helps explain why global ET trend studies have reported discrepant results, as the regions and magnitudes of disagreement can shift substantially with ensemble composition, study period, and spatial scale.

A clear example is the contrast between Yang et al. (2023), who reported a global increase in ET, and Kim et al. (2021), who found a decrease. In our analysis, most products show positive global annual ET trends, and six products exceed the 1.07 mm yr^{-2} maximum reported by Pan et al. (2020) for 1982–2011, with values ranging from 1.31 to 4.06 mm yr^{-2} over 2000–2019. In that sense, some products do support the interpretation of accelerated terrestrial evapotranspiration. However, the topology framework shows that several of these products, especially the GLDAS family and CAMELE, occupy systematic ensemble roles as signal boosters, while GLDAS-VIC v2.1 and GLDAS-NOAH v2.1 also act as signal opposers by generating significant trends where the ensemble majority does not. The discrepancy between increasing and decreasing global ET estimates is strongly affected by the products that exert disproportionate influence within the ensemble, beyond the reported mean ET trend values. If all products are treated as equally plausible, strong claims about accelerated global ET should be made with caution.

The prominence of the GLDAS family in these results also points to a second issue that is not captured by trend statistics alone, namely product genealogy. GLDAS-CLSM, GLDAS-NOAH, and GLDAS-VIC are not fully independent estimates, but closely related products that share the same atmospheric forcing and differ mainly in land surface model physics. More broadly, several ET datasets in our ensemble are linked through common forcing data, model structures, calibration sources, or direct compositing. FLDAS partly overlaps with GLDAS through its NOAH lineage, while CAMELE and SynthesizedET explicitly merge information from other ET products. Non-independence may also arise through shared calibration and validation targets. Several ET datasets, including MOD16, BESS, GLEAM, and ETMonitor, rely on FLUXNET observations for training, tuning, or evaluation, introducing an additional source of convergence across products. As a result, apparent agreement among products cannot always be interpreted as independent confirmation, because part of that agreement may reflect shared ancestry rather than genuinely distinct lines of evidence.

This perspective complements the topology framework. Topology shows which datasets systematically amplify, dampen, or oppose ensemble trends, whereas genealogy helps explain why some of these behaviors cluster within related product families. In this sense, equal treatment of all products may overstate the effective size of the ensemble and give disproportionate influence to particular lineages, by creating multiplicity artifacts (Vargas Godoy et al., 2025). The issue has already been identified in climate model ensembles, where spread within one model family does not remove structural differences across models with different process formulations (Tebaldi and Knutti, 2007). For ET products, this means that inter-product spread and opposition should be interpreted together with lineage, because some ensemble behavior may reflect multiplicity of related products rather than multiplicity of independent evidence. This motivates a broader consideration of ensemble dependence, where structured product roles may be reinforced by shared lineage, forcing, or benchmarking across datasets.

We further stress the caution raised by Miralles et al. (2016) regarding the use of single products in large-scale applications, while noting that robust checks to identify problematic datasets are still urgently needed. Our results show that substantial differences can arise even when a single product is used for regional studies, including assessments of ET trends, climate controls, and drivers. The topology framework reveals that disagreement within ET ensembles is not evenly distributed across datasets, but instead reflects structured behavioral roles. As a result, selecting a single ET product may lead to systematic overestimation, underestimation, or even directional disagreement in regional trend assessments. The GLEAM case study further shows that datasets with only moderate global topology ranks can still produce strong regional opposition to the ensemble trend signal (Figure 6), highlighting that product choice matters not only because datasets differ, but because they differ in regionally contingent ways.

The strong product dependence in ET trend estimates highlights how difficult it remains to reach consensus across datasets. These discrepancies affect not only the interpretation of recent ET change, but also confidence in the diverse methodological frameworks underlying current ET products, including empirical retrieval schemes, machine-learning approaches, and process-based representations. Although Or (2020) cautioned against the “tyranny of small scales” and argued that empirical approximations may remain valid in large-scale land surface models, substantial disagreement in trend magnitude and direction still raises the question of which ET-relevant processes, controls, or empirical relationships are being captured inconsistently across products. Our analysis focused on the empirical evidence of recent ET changes, but an important next step is to examine how these discrepancies propagate into inferred climate controls on ET variability. Distinguishing whether disagreement arises from input data, model structure, or algorithmic design is difficult from multi-product comparison alone. A useful extension would be to build on Pan et al. (2020), who attributed interannual ET variability using ensemble means from selected machine-learning, remote-sensing, and land-surface-model products, and identified distinct spatial patterns of precipitation, radiation, and temperature controls.

At the same time, a practical next step is to move topology from a diagnostic framework to a decision framework for ET ensemble design. Rather than treating all products as equally informative, topology roles could classify datasets within each region into core and conditional groups based on their tendency to dampen, amplify or oppose ensemble trend signals. Core products would define a conservative default ensemble, while conditional products, such as persistent trend opposers or significance opposers, would be retained mainly for sensitivity testing rather than baseline inference. For example, in WCE, GLDAS-VIC ranks among the strongest negative boosters, significance opposers, and opposition contributors (Figure 5), suggesting that it should not be treated as a neutral ensemble member when defining the default regional trend signal. In other regions, however, the same product may occupy a less oppositional role and therefore remain suitable for inclusion in a core ensemble. Such an approach would support fitness-for-purpose ensemble construction, recognizing that robust trend detection, hotspot identification, and attribution analyses may each require different product combinations and different tolerance for oppositional behavior.

More fundamentally, these results suggest that ET data products should be understood not only by the amount of disagreement they contain, but also by the way that disagreement is organized among them. The topology framework was developed to make this internal structure visible. In doing so, it shifts the focus from uncertainty as spread alone to uncertainty as a property of a multi-dataset ensemble. This perspective may be useful well beyond evapotranspiration. Across hydroclimatic research, data ensembles are routinely and increasingly used to infer change, identify hotspots, and support attribution, yet their members are often treated as broadly comparable and independent by default. Our results suggest that this assumption can be misleading. Making structural roles explicit offers a path toward more transparent, more critical, and ultimately more informative use of hydroclimatic data products.

5 Code availability

All code used for data processing, trend estimation, topology analysis, and figure generation is publicly available at https://github.com/jorub/ithaca/tree/main/projects/trend_evap. A permanent archived version will be provided upon acceptance.

6 Data availability

All original ET products used in this study are publicly available through their respective providers and can be accessed using the evapoRe R package (Ziveh et al., 2023), except for MOD16A2, which can be downloaded using the MODISTools R package (Hufkens and Labs, 2023).

The harmonized annual ET datasets used for trend estimation are available at https://doi.org/10.5281/zenodo.18150992 (Thomson et al., 2026a).

The spatial masks used in the analysis, including IPCC reference regions, elevation classes, ET quantiles, and Köppen–Geiger climate classifications ("evap_mask.csv"), are available at https://doi.org/10.5281/zenodo.14331232 (Thomson et al., 2026b).

All processed gridded trend estimates, topology metrics, and figure source data are available at https://doi.org/10.5281/zenodo.19843461 (Thomson, 2026).

Author contributions. J.R.T. and Y.M. designed the study and wrote the manuscript, J.R.T., performed the analyses, and prepared the figures and tables, J.R.T., Y.M., R.D., S.F., M.H. A.K., P.M., V.T., M.R.V.G., and A.P. contributed to the study introduction, discussion and to the manuscript editing. J.R.T. and V.T. collected and summarized detailed dataset information.

Competing interests. The authors declare that they have no conflict of interest

Acknowledgements. The authors would like to thank Akbar Rahmati Ziveh for help with downloading the evapotranspiration data. This work was carried out within the project "Investigation of Terrestrial HydrologicAl Cycle Acceleration (ITHACA)" funded by the Czech Science Foundation (Grant 22-33266M).

References

Abatzoglou, J. T., Dobrowski, S. Z., Parks, S. A., and Hegewisch, K. C.: TerraClimate, a high-resolution global dataset of monthly climate and climatic water balance from 1958–2015, Scientific Data, 5, 170 191, https://doi.org/10.1038/sdata.2017.191, number: 1 Publisher: Nature Publishing Group, 2018.

Anabalón, A. and Sharma, A.: On the divergence of potential and actual evapotranspiration trends: An assessment across alternate global datasets, Earth's Future, 5, 905–917, https://doi.org/10.1002/2016EF000499, _eprint: https://onlinelibrary.wiley.com/doi/pdf/10.1002/2016EF000499, 2017.

Beaudoing, H. and Rodell, M.: GLDAS Noah Land Surface Model L4 monthly 0.25 x 0.25 degree Early Product V2.1 (GLDAS_NOAH025_M_EP) at GES DISC, https://doi.org/https://doi.org/10.1175/BAMS-85-3-381, 2020.

Beaudoing, H., Rodell, M., and NASA/GSFC/HSL: GLDAS VIC Land Surface Model L4 monthly 1.0 x 1.0 degree V2.1, Greenbelt, Maryland, USA, Goddard Earth Sciences Data and Information Services Center (GES DISC)., https://doi.org/10.5067/VWTH7S6218SG, 2020.

Beck, H. E., Vergopolan, N., Pan, M., Levizzani, V., van Dijk, A. I. J. M., Weedon, G. P., Brocca, L., Pappenberger, F., Huffman, G. J., and Wood, E. F.: Global-scale evaluation of 22 precipitation datasets using gauge observations and hydrological modeling, Hydrology and Earth System Sciences, 21, 6201–6217, https://doi.org/10.5194/hess-21-6201-2017, 2017.

Beck, H. E., Zimmermann, N. E., McVicar, T. R., Vergopolan, N., Berg, A., and Wood, E. F.: Present and future Köppen-Geiger climate classification maps at 1-km resolution, Scientific Data, 5, 180 214, https://doi.org/10.1038/sdata.2018.214, publisher: Nature Publishing Group, 2018.

Cai, Y., Xu, Q., Bai, F., Cao, X., Wei, Z., Lu, X., Wei, N., Yuan, H., Zhang, S., Liu, S., Zhang, Y., Li, X., and Dai, Y.: Reconciling Global Terrestrial Evapotranspiration Estimates From Multi-Product Intercomparison and Evaluation, Water Resources Research, 60, https://doi.org/10.1029/2024WR037608, 2024.

Carslaw, D. C. and Ropkins, K.: *openair* — An R package for air quality data analysis, Environmental Modelling & Software, 27-28, 52–61, https://doi.org/10.1016/j.envsoft.2011.09.008, 2012.

Elnashar, A., Wang, L., Wu, B., Zhu, W., and Zeng, H.: Synthesis of global actual evapotranspiration from 1982 to 2019, Earth System Science Data, 13, 447–480, https://doi.org/10.5194/essd-13-447-2021, publisher: Copernicus GmbH, 2021.

Ershadi, A., McCabe, M., Evans, J., Chaney, N., and Wood, E.: Multi-site evaluation of terrestrial evaporation models using FLUXNET data, Agricultural and Forest Meteorology, 187, 46–61, https://doi.org/10.1016/j.agrformet.2013.11.008, 2014.

Gelaro, R., McCarty, W., Suárez, M. J., Todling, R., Molod, A., Takacs, L., Randles, C. A., Darmenov, A., Bosilovich, M. G., Reichle, R., Wargan, K., Coy, L., Cullather, R., Draper, C., Akella, S., Buchard, V., Conaty, A., Silva, A. M. d., Gu, W., Kim, G.-K., Koster, R., Lucchesi, R., Merkova, D., Nielsen, J. E., Partyka, G., Pawson, S., Putman, W., Rienecker, M., Schubert, S. D., Sienkiewicz, M., and Zhao, B.: The Modern-Era Retrospective Analysis for Research and Applications, Version 2 (MERRA-2), Journal of Climate, 30, 5419–5454, https://doi.org/10.1175/JCLI-D-16-0758.1, publisher: American Meteorological Society Section: Journal of Climate, 2017.

Good, S. P., Noone, D., and Bowen, G.: Hydrologic connectivity constrains partitioning of global terrestrial water fluxes, Science, 349, 175–177, https://doi.org/10.1126/science.aaa5931, publisher: American Association for the Advancement of Science, 2015.

Gu, G. and Adler, R. F.: Observed variability and trends in global precipitation during 1979–2020, Climate Dynamics, 61, 131–150, https://doi.org/10.1007/s00382-022-06567-9, 2023.

Gulev, S. K., Thorne, P. W., Ahn, J., Dentener, F. J., Domingues, C. M., Gerland, S., Gong, D., Kaufman, D. S., Nnamchi, H. C., Quaas, J., Rivera, J. A., Sathyendranath, S., Smith, S. L., Trewin, B., von Schuckmann, K., and Vose, R. S.: Changing State of the Climate System, in: Changing State of the Climate System. In Climate Change 2021: The Physical Science Basis. Contribution of Working Group I to the Sixth Assessment Report of the Intergovernmental Panel on Climate Change, edited by Masson-Delmotte, V., Zhai, P., Pirani, A., Connors, S. L., Péan, C., Berger, S., Caud, N., Chen, Y., Goldfarb, L., Gomis, M. I., Huang, M., Leitzell, K., Lonnoy, E., Matthews, J. B. R., Maycock, T. K., Waterfield, T., Yelekçi, O., Yu, R., and Zhou, B., pp. 287–422, Cambridge University Press, Cambridge, United Kingdom and New York, NY, USA, https://doi.org/10.1017/9781009157896.004, 2023.

Hersbach, H., Bell, B., Berrisford, P., Hirahara, S., Horányi, A., Muñoz-Sabater, J., Nicolas, J., Peubey, C., Radu, R., Schepers, D., Simmons, A., Soci, C., Abdalla, S., Abellan, X., Balsamo, G., Bechtold, P., Biavati, G., Bidlot, J., Bonavita, M., De Chiara, G., Dahlgren, P., Dee, D., Diamantakis, M., Dragani, R., Flemming, J., Forbes, R., Fuentes, M., Geer, A., Haimberger, L., Healy, S., Hogan, R. J., Hólm, E., Janisková, M., Keeley, S., Laloyaux, P., Lopez, P., Lupu, C., Radnoti, G., de Rosnay, P., Rozum, I., Vamborg, F., Villaume, S., and Thépaut, J.-N.: The ERA5 global reanalysis, Quarterly Journal of the Royal Meteorological Society, 146, 1999–2049, https://doi.org/10.1002/qj.3803, 2020.

Hufkens, K. and Labs, B.: MODISTools: Interface to the 'MODIS Land Products Subsets' Web Services, https://cran.r-project.org/web/packages/MODISTools/index.html, 2023.

Iturbide, M., Gutiérrez, J. M., Alves, L. M., Bedia, J., Cerezo-Mota, R., Cimadevilla, E., Cofiño, A. S., Di Luca, A., Faria, S. H., Gorodetskaya, I. V., Hauser, M., Herrera, S., Hennessy, K., Hewitt, H. T., Jones, R. G., Krakovska, S., Manzanas, R., Martínez-Castro, D., Narisma, G. T., Nurhati, I. S., Pinto, I., Seneviratne, S. I., van den Hurk, B., and Vera, C. S.: An update of IPCC climate reference regions for subcontinental analysis of climate model data: definition and aggregated datasets, Earth System Science Data, 12, 2959–2970, https://doi.org/10.5194/essd-12-2959-2020, publisher: Copernicus GmbH, 2020.

Jung, M., Reichstein, M., Ciais, P., Seneviratne, S. I., Sheffield, J., Goulden, M. L., Bonan, G., Cescatti, A., Chen, J., de Jeu, R., Dolman, A. J., Eugster, W., Gerten, D., Gianelle, D., Gobron, N., Heinke, J., Kimball, J., Law, B. E., Montagnani, L., Mu, Q., Mueller, B., Oleson, K., Papale, D., Richardson, A. D., Roupsard, O., Running, S., Tomelleri, E., Viovy, N., Weber, U., Williams, C., Wood, E., Zaehle, S., and Zhang, K.: Recent decline in the global land evapotranspiration trend due to limited moisture supply, Nature, 467, 951–954, https://doi.org/10.1038/nature09396, 2010.

Jung, M., Koirala, S., Weber, U., Ichii, K., Gans, F., Camps-Valls, G., Papale, D., Schwalm, C., Tramontana, G., and Reichstein, M.: The FLUXCOM ensemble of global land-atmosphere energy fluxes, Scientific Data, 6, 74, https://doi.org/10.1038/s41597-019-0076-8, number: 1 Publisher: Nature Publishing Group, 2019.

Khan, M. S., Liaqat, U. W., Baik, J., and Choi, M.: Stand-alone uncertainty characterization of GLEAM, GLDAS and MOD16 evapotranspiration products using an extended triple collocation approach, Agricultural and Forest Meteorology, 252, 256–268, https://doi.org/10.1016/j.agrformet.2018.01.022, 2018.

Kim, S., Anabalón, A., and Sharma, A.: An Assessment of Concurrency in Evapotranspiration Trends across Multiple Global Datasets, Journal of Hydrometeorology, 22, 231–244, https://doi.org/10.1175/JHM-D-20-0059.1, 2021.

Kobayashi, S., Ota, Y., Harada, Y., Ebita, A., Moriya, M., Onoda, H., Onogi, K., Kamahori, H., Kobayashi, C., Endo, H., Miyaoka, K., and Takahashi, K.: The JRA-55 Reanalysis: General Specifications and Basic Characteristics, Journal of the Meteorological Society of Japan. Ser. II, 93, 5–48, https://doi.org/10.2151/jmsj.2015-001, 2015.

Li, B., Beaudoing, H., Rodell, M., and NASA/GSFC/HSL: GLDAS Catchment Land Surface Model L4 monthly 1.0 x 1.0 degree V2.1, Greenbelt, Maryland, USA, Goddard Earth Sciences Data and Information Services Center (GES DISC)., https://doi.org/10.5067/FOUXNLXFAZNY, 2020.

Li, B., Ryu, Y., Jiang, C., Dechant, B., Liu, J., Yan, Y., and Li, X.: BESSv2.0: A satellite-based and coupled-process model for quantifying long-term global land–atmosphere fluxes, Remote Sensing of Environment, 295, 113 696, https://doi.org/10.1016/j.rse.2023.113696, 2023.

Li, C., Liu, Z., Yang, W., Tu, Z., Han, J., Li, S., and Yang, H.: CAMELE: Collocation-Analyzed Multi-source Ensembled Land Evapotranspiration Data, Earth System Science Data, 16, 1811–1846, https://doi.org/10.5194/essd-16-1811-2024, publisher: Copernicus GmbH, 2024.

Li, W., Yao, Z., Qu, Y., Yang, H., Song, Y., Song, L., Wu, L., and Cui, Y.: A benchmark dataset for global evapotranspiration estimation based on FLUXNET2015 from 2000 to 2022, Earth System Science Data, 17, 3835–3855, https://doi.org/10.5194/essd-17-3835-2025, 2025.

Ma, N., Zhang, Y., and Szilagyi, J.: Water-balance-based evapotranspiration for 56 large river basins: A benchmarking dataset for global terrestrial evapotranspiration modeling, Journal of Hydrology, p. 130607, https://doi.org/10.1016/j.jhydrol.2024.130607, 2024.

Markonis, Y., Vargas Godoy, M. R., Pradhan, R. K., Pratap, S., Thomson, J. R., Hanel, M., Paschalis, A., Nikolopoulos, E., and Papalexiou, S. M.: Spatial partitioning of terrestrial precipitation reveals varying dataset agreement across different environments, Communications Earth & Environment, 5, 217, https://doi.org/10.1038/s43247-024-01377-9, number: 1, 2024.

Martens, B., Miralles, D. G., Lievens, H., van der Schalie, R., de Jeu, R. A. M., Fernández-Prieto, D., Beck, H. E., Dorigo, W. A., and Verhoest, N. E. C.: GLEAM v3: satellite-based land evaporation and root-zone soil moisture, Geoscientific Model Development, 10, 1903–1925, https://doi.org/10.5194/gmd-10-1903-2017, 2017.

Mastrotheodoros, T., Pappas, C., Molnar, P., Burlando, P., Keenan, T. F., Gentine, P., Gough, C. M., and Fatichi, S.: Linking plant functional trait plasticity and the large increase in forest water use efficiency, Journal of Geophysical Research: Biogeosciences, 122, 2393–2408, https://doi.org/10.1002/2017JG003890, 2017.

Mauder, M., Foken, T., and Cuxart, J.: Surface-Energy-Balance Closure over Land: A Review, Boundary-Layer Meteorology, 177, 395–426, https://doi.org/10.1007/s10546-020-00529-6, 2020.

McCabe, M. F., Rodell, M., Alsdorf, D. E., Miralles, D. G., Uijlenhoet, R., Wagner, W., Lucieer, A., Houborg, R., Verhoest, N. E. C., Franz, T. E., Shi, J., Gao, H., and Wood, E. F.: The future of Earth observation in hydrology, Hydrology and Earth System Sciences, 21, 3879–3914, https://doi.org/10.5194/hess-21-3879-2017, publisher: Copernicus GmbH, 2017.

McNally, A., Arsenault, K., Kumar, S., Shukla, S., Peterson, P., Wang, S., Funk, C., Peters-Lidard, C. D., and Verdin, J. P.: A land data assimilation system for sub-Saharan Africa food and water security applications, Scientific Data, 4, 170 012, https://doi.org/10.1038/sdata.2017.12, number: 1 Publisher: Nature Publishing Group, 2017.

Miralles, D. G., Jiménez, C., Jung, M., Michel, D., Ershadi, A., McCabe, M. F., Hirschi, M., Martens, B., Dolman, A. J., Fisher, J. B., Mu, Q., Seneviratne, S. I., Wood, E. F., and Fernández-Prieto, D.: The WACMOS-ET project - Part 2: Evaluation of global terrestrial evaporation data sets, Hydrology and Earth System Sciences, 20, 823–842, https://doi.org/10.5194/hess-20-823-2016, 2016.

Miralles, D. G., Bonte, O., Koppa, A., Baez-Villanueva, O. M., Tronquo, E., Zhong, F., Beck, H. E., Hulsman, P., Dorigo, W., Verhoest, N. E. C., and Haghdoost, S.: GLEAM4: global land evaporation and soil moisture dataset at 0.1° resolution from 1980 to near present, Scientific Data, 12, 416, https://doi.org/10.1038/s41597-025-04610-y, publisher: Nature Publishing Group, 2025.

Mu, Q., Zhao, M., and Running, S. W.: Improvements to a MODIS global terrestrial evapotranspiration algorithm, Remote Sensing of Environment, 115, 1781–1800, https://doi.org/10.1016/j.rse.2011.02.019, 2011.

Muñoz-Sabater, J., Dutra, E., Agustí-Panareda, A., Albergel, C., Arduini, G., Balsamo, G., Boussetta, S., Choulga, M., Harrigan, S., Hersbach, H., Martens, B., Miralles, D. G., Piles, M., Rodríguez-Fernández, N. J., Zsoter, E., Buontempo, C., and Thépaut, J.-N.: ERA5-Land: a state-of-the-art global reanalysis dataset for land applications, Earth System Science Data, 13, 4349–4383, https://doi.org/10.5194/essd-13-4349-2021, publisher: Copernicus GmbH, 2021.

Or, D.: The Tyranny of Small Scales—On Representing Soil Processes in Global Land Surface Models, Water Resources Research, 56, https://doi.org/10.1029/2019WR024846, _eprint: https://onlinelibrary.wiley.com/doi/pdf/10.1029/2019WR024846, 2020.

Pan, S., Pan, N., Tian, H., Friedlingstein, P., Sitch, S., Shi, H., Arora, V. K., Haverd, V., Jain, A. K., Kato, E., Lienert, S., Lombardozzi, D., Nabel, J. E. M. S., Ottlé, C., Poulter, B., Zaehle, S., and Running, S. W.: Evaluation of global terrestrial evapotranspiration using state-of-the-art approaches in remote sensing, machine learning and land surface modeling, Hydrology and Earth System Sciences, 24, 1485–1509, https://doi.org/10.5194/hess-24-1485-2020, 2020.

Paschalis, A., Bonetti, S., Guo, Y., and Fatichi, S.: On the Uncertainty Induced by Pedotransfer Functions in Terrestrial Biosphere Modeling, Water Resources Research, 58, https://doi.org/10.1029/2021WR031871, _eprint: https://onlinelibrary.wiley.com/doi/pdf/10.1029/2021WR031871, 2022.

Pastorello, G., Trotta, C., Canfora, E., Chu, H., Christianson, D., Cheah, Y.-W., Poindexter, C., Chen, J., Elbashandy, A., Humphrey, M., Isaac, P., Polidori, D., Reichstein, M., Ribeca, A., van Ingen, C., Vuichard, N., Zhang, L., Amiro, B., Ammann, C., Arain, M. A., Ardö, J., Arkebauer, T., Arndt, S. K., Arriga, N., Aubinet, M., Aurela, M., Baldocchi, D., Barr, A., Beamesderfer, E., Marchesini, L. B., Bergeron, O., Beringer, J., Bernhofer, C., Berveiller, D., Billesbach, D., Black, T. A., Blanken, P. D., Bohrer, G., Boike, J., Bolstad, P. V., Bonal, D., Bonnefond, J.-M., Bowling, D. R., Bracho, R., Brodeur, J., Brümmer, C., Buchmann, N., Burban, B., Burns, S. P., Buysse, P., Cale, P., Cavagna, M., Cellier, P., Chen, S., Chini, I., Christensen, T. R., Cleverly, J., Collalti, A., Consalvo, C., Cook, B. D., Cook, D., Coursolle, C., Cremonese, E., Curtis, P. S., D'Andrea, E., da Rocha, H., Dai, X., Davis, K. J., Cinti, B. D., Grandcourt, A. d., Ligne, A. D., De Oliveira, R. C., Delpierre, N., Desai, A. R., Di Bella, C. M., Tommasi, P. d., Dolman, H., Domingo, F., Dong, G., Dore, S., Duce, P., Dufrêne, E., Dunn, A., Dušek, J., Eamus, D., Eichelmann, U., ElKhidir, H. A. M., Eugster, W., Ewenz, C. M., Ewers, B., Famulari, D., Fares, S., Feigenwinter, I., Feitz, A., Fensholt, R., Filippa, G., Fischer, M., Frank, J., Galvagno, M., Gharun, M., Gianelle, D., Gielen, B., Gioli, B., Gitelson, A., Goded, I., Goeckede, M., Goldstein, A. H., Gough, C. M., Goulden, M. L., Graf, A., Griebel, A., Gruening, C., Grünwald, T., Hammerle, A., Han, S., Han, X., Hansen, B. U., Hanson, C., Hatakka, J., He, Y., Hehn, M., Heinesch, B., Hinko-Najera, N., Hörtnagl, L., Hutley, L., Ibrom, A., Ikawa, H., Jackowicz-Korczynski, M., Janouš, D., Jans, W., Jassal, R., Jiang, S., Kato, T., Khomik, M., Klatt, J., Knohl, A., Knox, S., Kobayashi, H., Koerber, G., Kolle, O., Kosugi, Y., Kotani, A., Kowalski, A., Kruijt, B., Kurbatova, J., Kutsch, W. L., Kwon, H., Launiainen, S., Laurila, T., Law, B., Leuning, R., Li, Y., Liddell, M., Limousin, J.-M., Lion, M., Liska, A. J., Lohila, A., López-Ballesteros, A., López-Blanco, E., Loubet, B., Loustau, D., Lucas-Moffat, A., Lüers, J., Ma, S., Macfarlane, C., Magliulo, V., Maier, R., Mammarella, I., Manca, G., Marcolla, B., Margolis, H. A., Marras, S., Massman, W., Mastepanov, M., Matamala, R., Matthes, J. H., Mazzenga, F., McCaughey, H., McHugh, I., McMillan, A. M. S., Merbold, L., Meyer, W., Meyers, T., Miller, S. D., Minerbi, S., Moderow, U., Monson, R. K., Montagnani, L., Moore, C. E., Moors, E., Moreaux, V., Moureaux, C., Munger, J. W., Nakai, T., Neirynck, J., Nesic, Z., Nicolini, G., Noormets, A., Northwood, M., Nosetto, M., Nouvellon, Y., Novick, K., Oechel, W., Olesen, J. E., Ourcival, J.-M., Papuga, S. A., Parmentier, F.-J., Paul-Limoges, E., Pavelka, M., Peichl, M., Pendall, E., Phillips, R. P., Pilegaard, K., Pirk, N., Posse, G., Powell, T., Prasse, H., Prober, S. M., Rambal, S., Rannik, , Raz-Yaseef, N., Rebmann, C., Reed, D., Dios, V. R. d., Restrepo-Coupe, N., Reverter, B. R., Roland, M., Sabbatini, S., Sachs, T., Saleska, S. R., Sánchez-Cañete, E. P., Sanchez-Mejia, Z. M., Schmid, H. P., Schmidt, M., Schneider, K., Schrader, F., Schroder, I., Scott, R. L., Sedlák, P., Serrano-Ortíz, P., Shao, C., Shi, P., Shironya, I., Siebicke, L., Šigut, L., Silberstein, R., Sirca, C., Spano, D., Steinbrecher, R., Stevens, R. M., Sturtevant, C., Suyker, A., Tagesson, T., Takanashi, S., Tang, Y., Tapper, N., Thom, J., Tomassucci, M., Tuovinen, J.-P., Urbanski, S., Valentini, R., van der Molen, M., van Gorsel, E., van Huissteden, K., Varlagin, A., Verfaillie, J., Vesala, T., Vincke, C., Vitale, D., Vygodskaya, N., Walker, J. P., Walter-Shea, E., Wang, H., Weber, R., Westermann, S., Wille, C., Wofsy, S., Wohlfahrt, G., Wolf, S., Woodgate, W., Li, Y., Zampedri, R., Zhang, J., Zhou, G., Zona, D., Agarwal, D., Biraud, S., Torn, M., and Papale, D.: The FLUXNET2015 dataset and the ONEFlux processing pipeline for eddy covariance data, Scientific Data, 7, 225, https://doi.org/10.1038/s41597-020-0534-3, publisher: Nature Publishing Group, 2020.

Ruan, F., Yang, Y., Tu, Z., Xiong, J., and Guo, H.: Global evaluation of terrestrial evaporation trend from diagnostic products, Journal of Hydrology, 655, 132 979, https://doi.org/10.1016/j.jhydrol.2025.132979, 2025.

Schulzweida, U.: CDO User Guide, https://doi.org/10.5281/zenodo.10020800, 2023.

Tang, R., Peng, Z., Liu, M., Li, Z.-L., Jiang, Y., Hu, Y., Huang, L., Wang, Y., Wang, J., Jia, L., Zheng, C., Zhang, Y., Zhang, K., Yao, Y., Chen, X., Xiong, Y., Zeng, Z., and Fisher, J. B.: Spatial-temporal patterns of land surface evapotranspiration from global products, Remote Sensing of Environment, 304, 114 066, https://doi.org/10.1016/j.rse.2024.114066, 2024.

Tebaldi, C. and Knutti, R.: The use of the multi-model ensemble in probabilistic climate projections, Philosophical transactions of the royal society A: mathematical, physical and engineering sciences, 365, 2053–2075, 2007.

Thomson, J.: Agreement, opposition, and dataset influence in global evapotranspiration trends, https://doi.org/10.5281/zenodo.19843461, 2026.

Thomson, J., Dutta, R., and Markonis, Y.: Annual evapotranspiration data, https://doi.org/10.5281/zenodo.18150992, 2026a.

Thomson, J. R., Dutta, R., Markonis, Y., Vargas Godoy, M. R., Thakur, V., Greve, P., and Paschalis, A.: Mapping dataset agreement of global evapotranspiration datasets, https://doi.org/10.5281/zenodo.18151961, 2026b.

Vargas Godoy, M. R. and Markonis, Y.: PRecipe: A global precipitation climatology toolbox and database, Environmental Modelling & Software, 165, 105 711, 2023.

Vargas Godoy, M. R., Markonis, Y., Thomson, J. R., Ballarin, A. S., Perri, S., Miao, C., Sun, Q., Hanel, M., Papalexiou, S. M., Kummerow, C., Oki, T., and Molini, A.: Which Precipitation Dataset to Choose for Hydrological Studies of the Terrestrial Water Cycle?, Bulletin of the American Meteorological Society, 106, E2000–E2016, https://doi.org/10.1175/BAMS-D-24-0306.1, publisher: American Meteorological Society Section: Bulletin of the American Meteorological Society, 2025.

Wang, K. and Dickinson, R.: A review of global terrestrial evapotranspiration: Observation, modeling, climatology, and climatic variability, Reviews of Geophysics, 50, https://doi.org/10.1029/2011RG000373, 2012.

Yang, Y., Roderick, M. L., Guo, H., Miralles, D. G., Zhang, L., Fatichi, S., Luo, X., Zhang, Y., McVicar, T. R., Tu, Z., Keenan, T. F., Fisher, J. B., Gan, R., Zhang, X., Piao, S., Zhang, B., and Yang, D.: Evapotranspiration on a greening Earth, Nature Reviews Earth & Environment, 4, 626–641, https://doi.org/10.1038/s43017-023-00464-3, 2023.

Zhang, K., Kimball, J. S., Nemani, R. R., Running, S. W., Hong, Y., Gourley, J. J., and Yu, Z.: Vegetation Greening and Climate Change Promote Multidecadal Rises of Global Land Evapotranspiration, Scientific Reports, 5, https://doi.org/10.1038/srep15956, 2015.

Zhang, X., Zhang, Y., Tian, J., Ma, N., and Wang, Y.-P.: CO2 fertilization is spatially distinct from stomatal conductance reduction in controlling ecosystem water-use efficiency increase, Environmental Research Letters, 17, https://doi.org/10.1088/1748-9326/ac6c9c, publisher: IOP Publishing, 2022.

Zhang, Y., Peña-Arancibia, J. L., McVicar, T. R., Chiew, F. H. S., Vaze, J., Liu, C., Lu, X., Zheng, H., Wang, Y., Liu, Y. Y., Miralles, D. G., and Pan, M.: Multi-decadal trends in global terrestrial evapotranspiration and its components, Scientific Reports, 6, 19 124, https://doi.org/10.1038/srep19124, 2016.

Zheng, C., Jia, L., and Hu, G.: Global land surface evapotranspiration monitoring by ETMonitor model driven by multi-source satellite earth observations, Journal of Hydrology, 613, 128 444, https://doi.org/10.1016/j.jhydrol.2022.128444, 2022.

Ziveh, A. R., Godoy, M. R. V., Thakur, V., and Markonis, Y.: evapoRe: Evapotranspiration R Recipes, https://cran.r-project.org/web/packages/evapoRe/index.html, 2023.

Ziveh, A. R., Vargas Godoy, M. R., Thakur, V., Thomson, J. R., Hanel, M., and Markonis, Y.: evapoRe: An R-based application for exploratory data analysis of evapotranspiration, Environmental Modelling & Software, p. 106884, https://doi.org/10.1016/j.envsoft.2026.106884, 2026. 735